Geochemistry and zircon ages of the Yushigou diabase in the Longshoushan area, Alxa Block: implications for crust–mantle interaction and tectonic evolution

Original Article

Author for correspondence:
Jian-Qing Lai and Ren-Yu Zeng,
Emails: ljq@csu.edu.cn; zengrenyu@126.com

Ren-Yu Zeng[1,2,3] ![ORCID], Jian-Qing Lai[2,3], Xian-Cheng Mao[2,3], Jie Yan[1],
Chen-Guang Zhang[4] and Wen-Zhou Xiao[2,3] ![ORCID]

[1]State Key Laboratory of Nuclear Resources and Environment, East China University of Technology, Nanchang, 330013, Jiangxi, China; [2]Key Laboratory of Metallogenic Prediction of Nonferrous Metals and Geological Environment Monitoring, Ministry of Education, Central South University, Changsha 410083, China; [3]School of Geosciences and Info-Physics, Central South University, Changsha 410083, China and [4]College of Geographic Science, Xinyang Normal University, Xinyang, Henan, 464000, China

Abstract

The North Qilian orogenic belt in North China has been defined as a subduction–collision zone between the Alxa Block and the Qilian Block. We present petrography, zircon U–Pb geochronology, major- and trace-element geochemistry, and Sr–Nd–Pb–Hf isotope analysis for the Yushigou diabase from the Longshoushan area, which is located SW of the Alxa Block, aiming to understand its petrogenetic link to subduction processes. The Yushigou diabase belongs to the tholeiite series, and shows enrichment in light rare earth and large-ion lithophile elements, and a depletion in heavy rare earth and high-field-strength elements. Laser ablation – inductively coupled plasma – mass spectrometry U–Pb zircon dating yielded an emplacement age of 414 ± 9 Ma, with an $\epsilon_{Hf}(t)$ value in the range of -10.3 to 1.8. The whole-rock initial $^{206}Pb/^{204}Pb$, $^{207}Pb/^{204}Pb$ and $^{208}Pb/^{204}Pb$ ratios of the diabase range over 16.811–17.157, 15.331–15.422 and 37.768–37.895, respectively. The $(^{87}Sr/^{86}Sr)_i$ ratios vary between 0.7086 and 0.7106, and $\epsilon_{Nd}(t)$ values vary between -14.4 and -13.4, which are significantly higher than the $\epsilon_{Hf}(t)$ value (Nd–Hf decoupling). An interpretation of the elemental and isotopic data suggests that the Yushigou diabase was derived from partial melting of an enriched mantle I (EM-I) -type lithospheric mantle in the spinel–garnet transitional zone. Based on the geochemical features and previous regional geological data, we propose that the Silurian magmatism was most likely triggered by slab break-off after the closure of the North Qilian Ocean, and ancient continental materials from the subduction slab metasomatized the overlying lithospheric mantle during exhumation.

1. Introduction

As a part of the Qilian orogenic belt, the North Qilian orogenic belt (NQOB) is a typical early Palaeozoic accretionary orogenic belt located between the Alxa Block and the Central Qilian Block (Fig. 1a). The 550–450 Ma Yushigou, Jiugequan and Dachadaban ophiolite complexes confirm the existence of the North Qilian Ocean (Song *et al.* 2013; Xia *et al.* 2016). An abundant amount of 517–446 Ma arc magmatic rocks are exposed in the NQOB (Fig. 1b), indicating the N-wards subduction or bidirectional subduction of the North Qilian oceanic slab (Wang *et al.* 2005, 2017; Wu *et al.* 2010; Xia *et al.* 2012, 2016). Similar results are observed from the metamorphic age of eclogites (489–463 Ma, Song *et al.* 2004; Zhang *et al.* 2007) and the high-grade blueschists (467–445 Ma, Liu *et al.* 2006; Lin & Zhang, 2012; Cheng *et al.* 2016). Evidence, such as the widespread incipient Silurian molasse unconformably overlying the pre-Silurian strata in the Qilianshan area (Song *et al.* 2013; Xia *et al.* 2016), the latest arc volcanic magmatic activities (446 Ma, Wang *et al.* 2005) and the 465–440 Ma syn-collisional magmatism (adakite and S-type granite) (Chen *et al.* 2012; Yu *et al.* 2015), suggests that the final closure of the North Qilian Ocean and collision of the Alxa Block and Central Qilian Block took place during the Late Ordovician period. Subsequently, the NQOB entered an episode of intraplate evolution.

Studies have shown that subduction zones play an important role in the study of crust–mantle interaction and lithospheric mantle evolution (Goodenough *et al.* 2002; Ma *et al.* 2014). Fluids and/or melts that were released from the subduction plate would lead to the metasomatism of the overlying lithospheric mantle. However, studies of the compositions and evolution of the lithospheric mantle of the NQOB during the early Palaeozoic period are relatively sparse.

The Longshoushan area extends as a long narrow strip at the SW of the Alxa Block, which is directly connected to the NQOB on the south side. There are extensive intrusions of the early Palaeozoic igneous rocks in the Longshoushan area (Duan *et al.* 2015; Zeng *et al.* 2016; Zhao
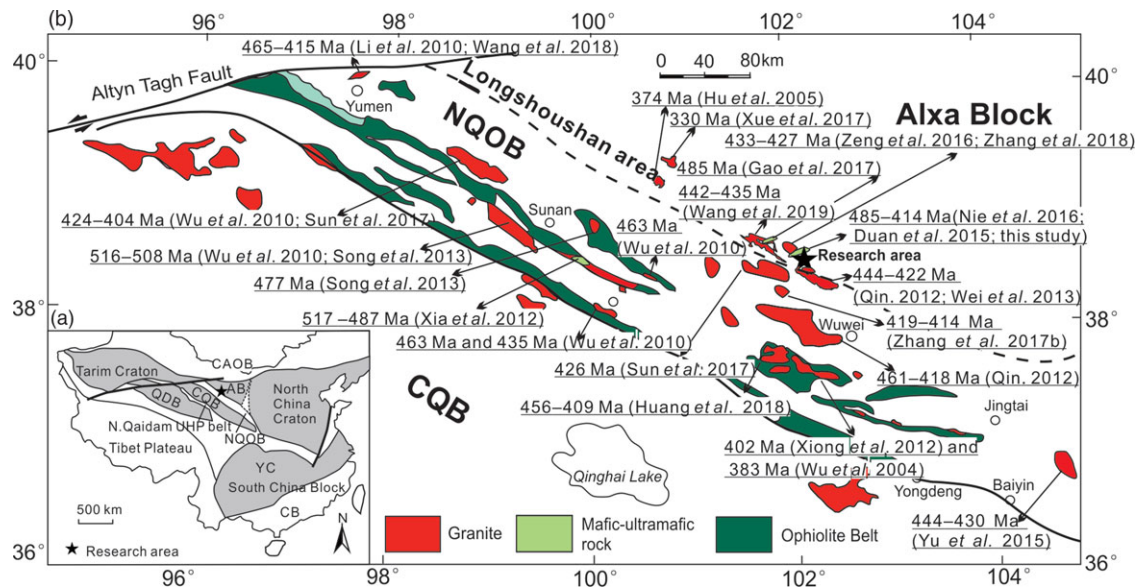
Fig. 1. (Colour online) (a) Tectonic units of China (after Song *et al*. 2013). (b) Geological map of the NQOB and the southern margin of Alxa Block (modified from Song *et al*. 2013). YC –Yangtze Craton; CB – Cathaysian Block; AB – Alxa Block; CQB – Central Qilian Block; QDB – Qaidam Block; CAOB – Central Asian Orogenic Belt; NQOB – North Qilian Orogenic Belt; N. Qaidam UHP belt – North Qaidam ultrahigh-pressure metamorphic belt.

et al. 2016; Wang *et al*. 2019). Mafic–ultramafic magmas from the mantle can be used directly to reflect their magmatic sources and tectonic setting (Meng *et al*. 2014). However, previous studies focused on the widely exposed granitoid rocks, and were not concerned with the mafic rocks. Only Gao *et al*. (2017) and Duan *et al*. (2015) reported two early Palaeozoic mafic rocks in the Longshoushan area, but these studies pay less attention to the composition of their mantle source. In this paper, we present an integrated study of geology and petrology with zircon U–Pb–Hf isotopes and whole-rock geochemistry (major- and trace-element analysis, and Sr–Nd–Pb isotopic compositions) on the Yushigou diabase from the central Longshoushan area to precisely determine the age, petrogenesis and mantle source of the diabase. Combined with the available mafic rock information in the research area, we evaluate the nature and evolution of mantle sources and the geodynamic setting of the Longshoushan area during the early Palaeozoic period.

2. Geological setting and petrology

The Longshoushan, the study area extends in an NWW–SEE direction and is located in the SW of the Alxa Block. This area is bounded by faults to the south against the NQOB (Fig. 1) and known for the Jinchuan deposit, the third-largest copper-nickel sulphide deposit in the world.

The Longshoushan area consists primarily of outcrops of the Mesoarchean–Palaeoproterozoic Longshoushan Complex (Gong *et al*. 2016; Zeng *et al*. 2018), the late Mesoproterozoic Dunzhigou Group (Xu & Jiang, 2003) and the Neoproterozoic–Cambrian Hanmushan Group (Xie *et al*. 2013). As the basement rock, the NWW-striking Longshoushan Complex is exposed in a long narrow belt that is approximately 500 km long and 30 km wide (Tung *et al*. 2007). It is in unconformable contact with the overlying strata of the Dunzhigou Group. The Longshoushan Complex underwent strong deformation, low-amphibolite facies regional metamorphism and migmatization during the middle– late Orosirian period (Tung *et al*. 2007; Zeng *et al*. 2018). It mainly

consists of marbles, amphibolites, schists, leptynites and migmatites.

The extensive development of Palaeozoic magmatism is a major feature of the Longshoushan area. These Palaeozoic magmatic rocks can be roughly divided into two stages: *c.* 485 Ma and 445–414 Ma. The *c.* 485 Ma magmatic rocks, consisting mainly of intermediate and mafic rocks, are exposed at the Jiling in the central region of the Longshoushan area (Nie *et al*. 2016; Gao *et al*. 2017). The 445–414 Ma felsic rocks widely occur in the Longshoushan area, with high contents of potassium and sodium, and most of them belong to the alkaline series (Zhao *et al*. 2016; Zeng *et al*. 2016; Zhang *et al*. 2017*b*; Wang *et al*. 2019). In addition, the 424–421 Ma Jinchang diabase (Duan *et al*. 2015) and the mafic microgranular enclaves (MMEs) in the 442–435 Ma Jiling pluton (Wang *et al*. 2019) indicate that there is a small amount of mantle-derived magmatism in the Longshoushan area. Since then, a small number of Middle Devonian – middle Permian magmatic rocks have been sporadically exposed in the Longshoushan area, such as the 374 Ma Zhigoumen pluton (Hu *et al*. 2005), the 361 Ma Jinchang granite porphyry (Zeng *et al*. 2016), the 330 Ma Taohualashan granite (Xue *et al*. 2017) and the 280 Ma Xiaokouzi mafic–ultramafic rocks (Jiao *et al*. 2017). In the Longshoushan area, the Early Palaeozoic and Devonian magmatic events are generally associated with the evolution of the NQOB (Hu *et al*. 2005; Wei *et al*. 2013; Duan *et al*. 2015; Zeng *et al*. 2016; Zhang *et al*. 2017*a*, *b*, 2018). The small amount of 330– 230 Ma magmatic rocks are considered to have formed under the influence of the Central Asian orogenic belt (Jiao *et al*. 2017; Xue *et al*. 2017).

3. Field relationship and petrography

Diabase dykes are common throughout the Jinchuan mining area (Fig. 1), central to the Longshoushan area (Figs 1, 2), although these are generally smaller in size (approximately 3–30 m in width and 300–900 m in length). These dykes show two distinct orientations: N–W and N–E. The NW-trending Yushigou diabase dyke,
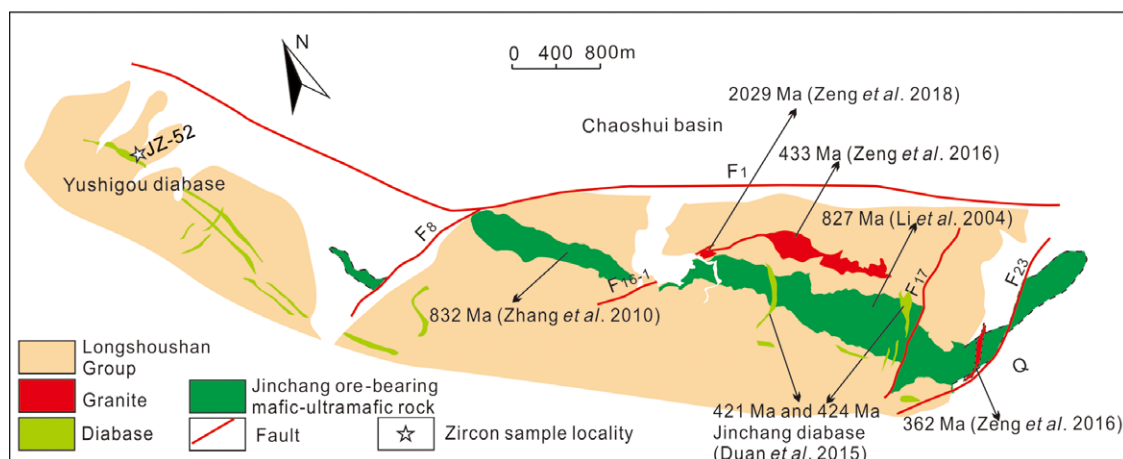
Fig. 2. (Colour online) Geological map of the Jinchuan mineral area.

which is 5–15 m wide and 600 m long, occurs *c.* 1 km NW of the *c.* 830 Ma Jinchuan ore-bearing mafic–ultramafic rock (Li *et al.* 2004; Zhang *et al.* 2010) and *c.* 5 km NW of the 424–421 Ma Jinchang diabase (Duan *et al.* 2015) (Fig. 2). It intrudes into the marble and migmatite of the Longshoushan Complex (Figs 2, 3a), which commonly have sharp contact (Fig. 3b).

The Yushigou diabase is generally yellow-green-grey in colour and has a characteristic diabasic texture (Fig. 3b). Compositionally, the rocks are mainly composed of plagioclase (*c.* 60 vol%), pyroxene (*c.* 30 vol%) and opaques (e.g. magnetite *c.* 10 vol%). The accessory phases include apatite and zircon. The plagioclase crystals are euhedral to subhedral, with grain sizes ranging between 0.6 mm and 0.8 mm (Fig. 3c). The pyroxene crystals are mainly anhedral and 0.1–0.4 mm in size, and they occur as interstitial grains between plagioclase. Most plagioclases have experienced sericitization, and some pyroxenes were altered to chlorite and amphibole. Twelve samples of the Yushigou diabase were collected along the strike of the diabase dyke on the surface. Each sample was collected from the centre of the diabase dyke. Zircon sample JZ-52 was obtained from one sample collected at the locations shown in Figure 2.

4. Analytical methods

4.a. Major- and trace-element analyses

A total of 11 fresh rock samples from the studied area were selected for geochemical analysis. Whole-rock major- and trace-element analyses (except for Pb and Ni contents) were determined at ALS Chemex (Guangzhou) Co. Ltd. Major oxide concentrations were measured by X-ray fluorescence (XRF) spectrometry. Fused glass disks with lithium borate were used and the analytical precision was better than ±0.01%, estimated from repeated analyses of the standards GSR-2 and GSR-3. Trace elements were detected using the lithium borate dissolution method and inductively coupled plasma – mass spectrometry (ICP-MS). Analyses of United States Geological Survey rock standards (BCR-2, BHVO-1 and AGV-1) indicate precision and accuracy are better than ±5% for trace elements.

Whole-rock element analyses of Pb and Ni for five samples (J7-1 to J7-6) were carried out at Nanjing FocuMS Technology Co. Ltd. Rock digestion diluent was nebulized into Agilent Technologies 7700× quadrupole ICP-MS (Hachioji, Tokyo, Japan) to determine

the trace elements. Geochemical reference materials of USGS – basalt (BIR-1, BCR-2, BHVO-2), andesite (AVG-2), rhyolite(RGM-2) and granodiorite(GSP-2) – were treated as quality control. Measured values of these reference materials were compared with preferred values in GeoReM database (http://georem.mpch-mainz.gwdg.de). Deviations were better than ±10% for the elements that exceeded 10 ppm and better than ±5% for the elements that exceeded 50 ppm.

4.b. Zircon U–Pb dating and Hf isotope analyses

Zircon U–Pb dating analyses were performed at the Key Laboratory of Crust–Mantle Materials and Environments of CAS at the University of Science and Technology of China (USTC), using a laser ablation (LA) (ICP-MS; Perkin Elmer Elan DRC II) equipped with a Microlas system (GeoLas 200 M, 193 nm ArFexcimer laser). Zircon 91500 and SRM610 were used as the external standards for U–Pb isotope ratios and element content, respectively. The spot diameter of laser ablation pits is 32 μm and the average power output about 4 W. For detailed instrument parameters and analysis processes, refer to Sun *et al.* (2013) and Gu *et al.* (2013).

In situ Hf ratio analyses were performed using the 193 nm ArF laser and Thermo Scientific Neptune multi-collector (MC) ICP-MS at the Advanced Analytical Centre at James Cook University. Spot sizes were 44 μm, with a 4 Hz laser pulse repetition rate. The analytical protocols were similar to those outlined in Næraa *et al.* (2012). The Mud Tank reference zircon (MTZ) and the Geostandard FC1 zircon were used as the external standards; the $^{176}Hf/^{177}Hf$ ratios of these two external standards are 0.282184 and 0.282507, respectively (Woodhead & Hergt, 2005). Standard zircon MTZ and FC1 were analysed in the experiment, and the $^{176}Hf/^{177}Hf$ ratios were 0.282148–0.282175 and 0.282488–0.282502, respectively, in accordance with the recommended value.

4.c. Sr–Nd–Pb isotopic analyses

High-precision isotopic (Sr, Nd, Pb) measurements were carried out at Nanjing FocuMS Technology Co. Ltd. The Sr-, Nd- and Pb-bearing elution was dried down and re-dissolved in 1.0 mL 2 wt% HNO_3. Small aliquots of each were analysed using Agilent Technologies 7700× quadrupole ICP-MS (Hachioji, Tokyo, Japan) to determine the exact contents of Sr, Nd and Pb
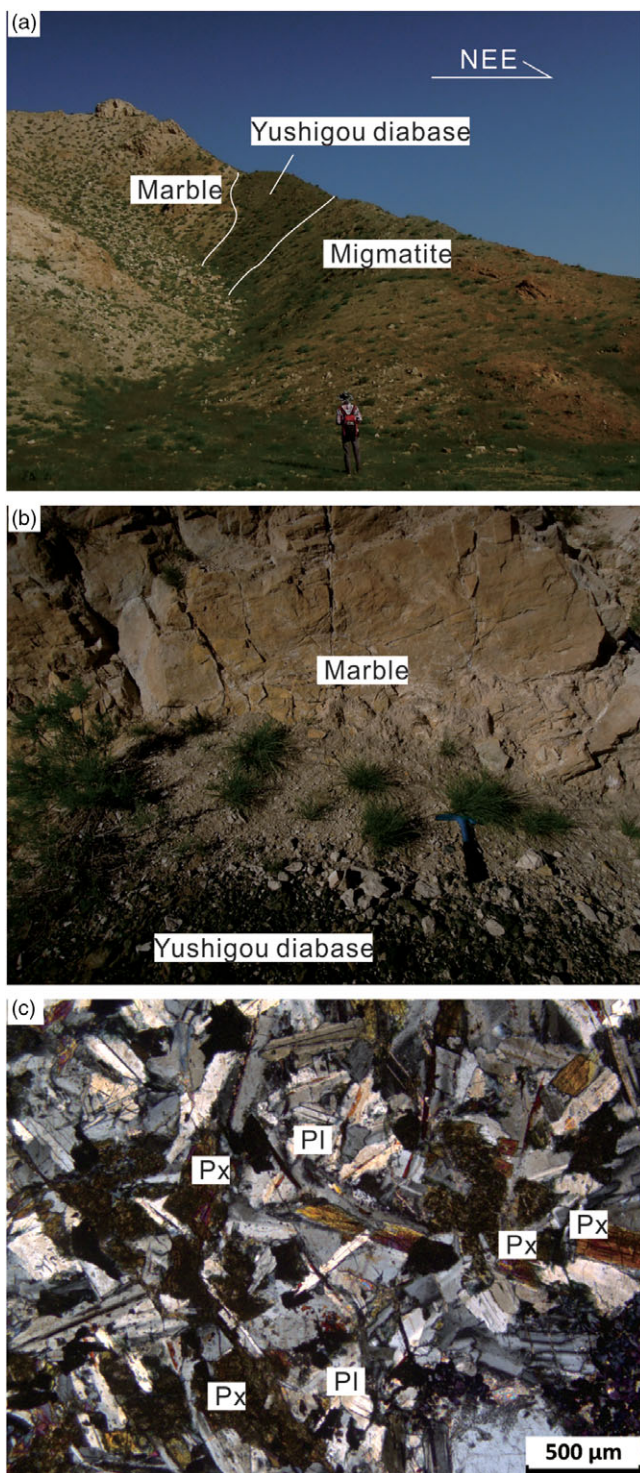
Fig. 3. (Colour online) Photographs and corresponding micrographs. (a) Diabase dyke intruding marble and migmatite of the Longshoushan Complex. (b) Contact between diabase and marble. (c) Diabasic texture (perpendicular polarized light). Mineral abbreviations: Px – pyroxene; Pl – plagioclase.

available. Raw data of isotopic ratios were corrected for mass fractionation by normalizing to $^{86}Sr/^{88}Sr = 0.1194$ for Sr, $^{146}Nd/^{144}Nd = 0.7219$ for Nd and $^{205}Tl/^{203}Tl = 2.3885$ for Pb with exponential law. In the experiment, repeat analyses yielded an $^{87}Sr/^{86}Sr$ ratio of 0.710240–0.710250 for the NBS-987 Sr standard, a $^{143}Nd/^{144}Nd$ ratio of 0.512111–0.512135 for the JNdi-1 Nd standard, and

a $^{204}Pb/^{206}Pb$ of 0.05902–0.05904, $^{207}Pb/^{206}Pb$ of 1.09277–1.09353 and $^{208}Pb/^{206}Pb$ of 2.16609–2.16711 for NBS981 Pb standard.

5. Analytical results

Tables 1–4 list the data for major and trace elements, zircon U–Pb ages, Hf isotopes and Sr–Nd–Pb isotopes, respectively.

5.a. Geochemical characteristics

Table 1 shows that 11 diabase samples have SiO_2 contents from 48.30 to 49.90 wt% and Al_2O_3 contents from 13.70 to 15.65 wt %. The contents of K_2O and Na_2O are 0.96–2.88 wt% and 2.40–2.93 wt%, respectively, with a Na_2O/K_2O ratio of 0.98–2.74. All samples fall in the gabbro and monzo-gabbro fields in the total alkali versus silica (TAS) diagram (Fig. 4a). The contents of MgO and FeO_{total} (FeO_{total} = all Fe calculated as Fe_2O_3) are 4.76–5.40 wt% and 13.16–14.64 wt%, respectively, with Mg no. values (Mg no. = molar (Mg×100)/(Mg+Fe)) of 41–44. All rocks are tholeiitic series in the FeO_T/MgO versus SiO_2 diagram (where FeO_T is all Fe calculated as FeO) (Fig. 4b).

The La_N/Yb_N values of the Yushigou diabase range from 8.54 to 10.16, showing enrichment of light rare earth elements (LREEs) and depletion of heavy rare earth elements (HREEs) (Fig. 5a). All samples display no clearly Eu anomalies (δEu = 0.97–1.09) and slight positive Ce anomalies (δCe = 1.02–1.08). In the primitive-mantle-normalized trace-element diagram (Fig. 5b), the samples show enrichment of La and large-ion lithophile elements (LILEs; e.g. Rb, Ba and K), and depletion of high-field-strength elements (HFSEs; e.g. Nb, Ta, Th, U and P).

In the Harker diagrams (Fig. 6), MgO is shown to be positively correlated with FeO_{total}, V and Ni, but has no correlation with Al_2O_3, TiO_2 and CaO.

5.b. Zircon U–Pb ages and Hf isotopes

Cathodoluminescence (CL) images of zircons from JZ-52 are shown in Figure 7a. The lengths of these zircons range from 60 to 110 μm and display either weak oscillatory or banded zoning in the CL images. In the U–Pb concordia diagram (Fig. 7b), 12 spots are clustered on the concordia curve of $^{206}Pb/^{238}U$ with ages of 398–442 Ma and Th/U ratios of 0.61–1.16, defining a weighted mean age of 414 ± 9 Ma (mean square weighted deviation or MSWD = 0.47).

Six zircons were analysed for Lu–Hf isotopes from sample JZ-52. By using the U–Pb age for each zircon, $^{176}Hf/^{177}Hf$ ratios and $\epsilon_{Hf}(t)$ values of 0.282232 to 0.282578 and −10.3 to 1.8, respectively, were determined.

5.c. Whole-rock Sr–Nd–Pb isotopes

The samples of the Yushigou diabase have $(^{206}Pb/^{204}Pb)_i$ ratios of 16.811–17.157, $(^{207}Pb/^{204}Pb)_i$ ratios of 15.331–15.422 and $(^{208}Pb/^{204}Pb)_i$ ratios of 37.768–37.895 (the initial isotope ratios of diabase, calculated for $t = 414$ Ma). They plot significantly above the North Hemisphere Reference Line (NHRL) and in or near the enriched mantle (EM-) I field in the $(^{207}Pb/^{204}Pb)_i$ versus $(^{206}Pb/^{204}Pb)_i$ and $(^{208}Pb/^{204}Pb)_i$ versus $(^{206}Pb/^{204}Pb)_i$ diagrams (Fig. 8a, b).

The samples of the Yushigou diabase have uniform $(^{87}Sr/^{86}Sr)_i$ ratios of 0.7086–0.7106 and $\epsilon_{Nd}(t)$ values of −14.4 to −13.4. As shown in the $\epsilon_{Nd}(t)$ versus $(^{87}Sr/^{86}Sr)_i$ diagram (Fig. 8c), the samples plot above the evolutionary trend defined by mid-ocean ridge basalt (MORB) and lower or middle continental crust (LCC/MCC)

Table 1. Major element (wt%) and trace element (ppm) compositions of the Yushigou diabase

Sample	JZ-48	JZ-49	JZ-50	JZ-53	JZ-54	JZ-56	J7-1	J7-2	J7-3	J7-5	J7-6
SiO_2	49.50	49.90	49.60	49.20	48.30	48.30	49.13	49.71	49.31	48.60	49.20
TiO_2	2.30	2.10	2.29	2.16	2.39	2.14	2.28	2.28	2.14	2.36	2.22
Al_2O_3	14.45	15.65	14.65	14.40	14.35	13.70	14.36	14.62	14.47	14.60	14.35
FeO_{total}	14.19	13.16	13.84	14.23	14.35	13.93	14.50	14.07	13.73	14.64	14.30
MnO	0.18	0.16	0.16	0.18	0.19	0.17	0.18	0.18	0.16	0.18	0.17
MgO	5.09	4.76	5.03	5.40	5.17	4.79	5.20	5.10	5.34	5.01	5.29
CaO	7.61	8.15	8.26	8.52	8.50	7.62	8.41	8.02	8.23	8.18	8.04
K_2O	1.34	1.33	1.12	0.96	1.30	2.88	1.08	1.22	1.74	1.12	1.77
Na_2O	2.79	2.74	2.68	2.63	2.73	2.83	2.82	2.85	2.60	2.93	2.40
P_2O_5	0.35	0.29	0.31	0.27	0.41	0.30	0.30	0.30	0.25	0.39	0.27
LOI	1.49	1.55	1.19	1.23	1.46	3.37	1.62	1.79	1.55	1.56	1.50
Mg no.	42	42	42	43	42	41	42	42	44	41	43
V	303	276	313	307	307	283	316	310	323	308	334
Cr	30	30	30	40	30	30	30	30	30	30	30
Ni	ND	ND	ND	ND	ND	ND	63.53	63.48	67.85	56.98	68.64
Ga	24.9	24.2	25.0	24.3	23.7	22.2	22.4	23.3	23.1	22.5	23.5
Rb	59.6	57.7	38.0	32.9	47.2	99.8	31.8	51.1	67.6	43.0	71.2
Sr	559.0	626.0	545.0	543.0	537.0	473.0	503	560	592	567	548
Y	29.0	25.8	29.2	27.5	27.9	26.1	28.0	29.2	28.4	30.1	28.5
Zr	226	193	212	200	213	193	198	205	191	228	194
Nb	16.7	14.4	16.3	15.2	15.7	14.7	14.5	15.2	14.8	16.3	14.7
Sn	3	2	2	2	2	2	1	1	2	1	1
Cs	0.39	0.48	0.74	0.35	0.30	0.52	0.52	0.55	0.47	0.39	0.41
Ba	466	497	493	401	548	986	492	558	653	576	768
Hf	5.2	4.4	5.3	4.8	4.9	4.7	4.9	4.9	4.7	5.4	4.8
Ta	1.0	0.8	0.9	0.9	0.8	0.8	0.9	0.8	0.9	0.9	0.8
W	2	1	4	1	2	2	4	1	1	1	1
Th	4.27	3.76	4.18	4.03	3.32	3.71	3.65	3.72	3.61	3.30	3.57
U	0.70	0.78	0.72	0.76	1.05	0.74	0.58	0.75	0.66	0.80	0.70
La	31.3	27.7	32.2	29.6	29.9	28.1	32.3	33.6	31.5	35.4	29.6
Ce	68.4	60.5	70.4	65.3	67.1	62.5	72.2	75.0	69.9	80.2	67.1
Pr	8.55	7.42	8.74	7.93	8.33	7.96	8.36	8.79	8.07	9.54	7.81
Nd	33.3	29.4	34.5	31.9	32.8	30.6	33.9	36.0	34.0	38.9	31.9
Sm	7.13	6.29	7.30	6.72	7.09	6.33	6.78	7.23	7.09	7.93	6.76
Eu	2.29	2.07	2.49	2.08	2.38	2.11	2.21	2.33	2.22	2.61	2.05
Gd	6.56	5.88	6.74	6.01	6.62	6.24	6.77	6.87	6.44	7.18	6.21
Tb	0.97	0.93	1.03	0.94	0.95	0.92	0.95	0.98	0.90	1.03	0.92
Dy	5.77	5.19	5.95	5.45	5.44	5.36	5.38	5.58	5.21	5.79	5.32
Ho	1.10	0.97	1.15	1.06	1.11	1.03	1.07	1.09	1.04	1.19	1.05
Er	3.03	2.69	3.14	2.75	2.90	2.78	2.81	2.92	2.81	3.17	2.79
Tm	0.42	0.38	0.43	0.42	0.41	0.38	0.38	0.40	0.38	0.43	0.39
Yb	2.63	2.18	2.47	2.40	2.41	2.28	2.28	2.45	2.34	2.60	2.33
Lu	0.37	0.33	0.36	0.37	0.37	0.37	0.35	0.38	0.36	0.40	0.35

(Continued)

Table 1. (*Continued*)

Sample	JZ-48	JZ-49	JZ-50	JZ-53	JZ-54	JZ-56	J7-1	J7-2	J7-3	J7-5	J7-6
Pb	ND	ND	ND	ND	ND	ND	43	27	31	33	25
ΣREE	171.82	151.93	176.90	162.93	167.81	156.96	175.74	183.62	172.26	196.37	164.58
La_N/Yb_N	8.54	9.11	9.35	8.85	8.90	8.84	10.16	9.84	9.66	9.77	9.11
δEu	1.02	1.04	1.09	1.00	1.06	1.03	1.00	1.01	1.00	1.06	0.97
δCe	1.03	1.03	1.03	1.04	1.04	1.02	1.08	1.07	1.07	1.07	1.08

Note: Mg no. = molar (Mg×100)/(Mg+Fe); FeO_{total} = all Fe calculated as Fe_2O_3; LOI – loss on ignition; ND – not determined. Whole-rock major- and trace-element analyses (except the Pb and Ni contents) were determined at ALS Chemex (Guangzhou) Co. Ltd.; Pb and Ni analyses of whole-rock for five samples (J7-1 to J7-6) were carried out at Nanjing FocuMS Technology Co. Ltd.

Table 2. Zircon LA-ICP-MS U–Pb isotopic data and ages of the Yushigou diabase

Analysis	Pb	Th $(\times10^{-6})$	U	Th/U	$^{207}Pb/^{206}Pb$ Ratio	1σ	$^{207}Pb/^{235}U$ Ratio	1σ	$^{206}Pb/^{238}U$ Ratio	1σ	$^{207}Pb/^{206}$P Age (Ma)	1σ	$^{207}Pb/^{235}U$ Age (Ma)	1σ	$^{206}Pb/^{238}U$ Age (Ma)	1σ
1	91	868	1004	0.86	0.05945	0.00272	0.55177	0.04447	0.06715	0.00289	583	105	446	29	419	17
3	82	849	938	0.90	0.05610	0.00272	0.50007	0.04199	0.06450	0.00282	456	100	412	28	403	17
5	110	1211	1127	1.08	0.05625	0.00260	0.53318	0.04367	0.06866	0.00305	462	96	434	29	428	18
6	11	86	118	0.73	0.05906	0.00410	0.56261	0.06177	0.06907	0.00335	569	150	453	40	431	20
8	84	621	995	0.62	0.05985	0.00290	0.52610	0.04473	0.06374	0.00290	598	104	429	30	398	18
9	17	160	178	0.90	0.05629	0.00380	0.51156	0.05487	0.06596	0.00316	464	139	419	37	412	19
12	42	412	440	0.94	0.06020	0.00312	0.53915	0.04863	0.06508	0.00309	611	106	438	32	406	19
13	62	632	570	1.11	0.05693	0.00273	0.51234	0.03732	0.06493	0.00241	489	101	420	25	406	12
15	64	627	540	1.16	0.05805	0.00286	0.54279	0.03903	0.06753	0.00305	532	106	440	26	421	18
17	91	764	772	0.99	0.06048	0.00216	0.59221	0.04377	0.07102	0.00314	621	74	472	29	442	21
18	21	150	248	0.61	0.05898	0.00248	0.53865	0.04442	0.06595	0.00202	566	89	438	31	412	13
19	8	61	84	0.73	0.06666	0.00212	0.60136	0.04013	0.06647	0.00207	827	65	478	26	415	12

Note: σ is mean square error.

Table 3. Zircon Hf isotopic data of the Yushigou diabase

Analysis	t (Ma)	$^{176}Yb/^{177}Hf$	$^{176}Lu/^{177}Hf$	$^{176}Hf/^{177}Hf$	2σ	$\epsilon_{Hf}(t)$	2σ	T_{DM1} (Ma)	T_{DM2} (Ma)
1	419	0.033187	0.000936	0.282232	0.000015	−10.13	0.53	1435	2046
3	403	0.022034	0.000655	0.282236	0.000014	−10.27	0.51	1420	2043
5	428	0.023104	0.000791	0.282236	0.000015	−9.76	0.52	1425	2030
6	431	0.051828	0.001739	0.282464	0.000017	−1.91	0.60	1136	1536
8	398	0.031061	0.001241	0.282414	0.000020	−4.23	0.72	1192	1658
9	412	0.042244	0.001473	0.282578	0.000017	1.80	0.62	966	1287

For the calculation of $\epsilon_{Hf}(t)$ values, we adopted the ^{176}Lu decay constant of 1.867×10^{-11} (Söderlund *et al.* 2004), and the present-day chondritic values of $^{176}Lu/^{177}Hf = 0.0332$ and $^{176}Hf/^{177}Hf = 0.282772$ (Blichert-Toft & Albarède, 1997). To calculate one-stage model ages (T_{DM1}) relative to a depleted-mantle source, we adopted the present-day depleted-mantle values of $^{176}Lu/^{177}Hf = 0.0384$ and $^{176}Hf/^{177}Hf = 0.28325$ (Vervoort & Blichert-Toft, 1999).

as well as near the EM-I field. As shown in the $\epsilon_{Nd}(t)$ versus $\epsilon_{Hf}(t)$ diagram (Fig. 8d), the samples plot significantly above the mantle array.

6. Discussion

6.a. Emplacement age

Zircons in mafic rocks are generally characterized by homogenous structures and/or banding and/or weak oscillatory zoning on CL images, while Th/U ratios (generally > 0.6, often > 1.0) are significantly higher than those of granitic igneous zircons (generally between 0.3 and 0.8) (Wang *et al.* 2011, 2016). Based on banded zoning or weak oscillatory zoning structures and high Th/U ratios (0.61–1.16; average, 0.88), the zircon grains from the Yushigou diabase can be ascribed to typical magmatic zircons crystallized from mafic rocks. In addition, the diabase dyke intrudes into the early Precambrian metamorphic basement, which is characterized by a large amount of Palaeoproterozoic zircon (Tung *et al.* 2007; Zeng *et al.* 2018). The youngest detrital zircon in the metamorphic

Table 4. Sr, Nd and Pb isotopic compositions of the Yushigou diabase

Sample	J7-1	J7-2	J7-3	J7-5	J7-6
Rb (ppm)	31.8	51.1	67.6	43.0	71.2
Sr (ppm)	503	560	592	567	548
$^{87}Rb/^{86}Sr$	0.1830	0.2641	0.3304	0.2195	0.3761
$^{87}Sr/^{86}Sr$	0.711202	0.712073	0.710534	0.711563	0.712851
2σ	0.000007	0.000007	0.000007	0.000008	0.000008
$(^{87}Sr/^{86}Sr)_i$	0.710126	0.710520	0.708591	0.710272	0.710639
Sm (ppm)	6.78	7.23	7.09	7.93	6.76
Nd (ppm)	33.9	36.0	34.0	38.9	31.9
$^{147}Sm/^{144}Nd$	0.1209	0.1214	0.1260	0.1232	0.1280
$^{143}Nd/^{144}Nd$	0.511730	0.511734	0.511760	0.511704	0.511756
2σ	0.000004	0.000006	0.000004	0.000004	0.000004
$(^{143}Nd/^{144}Nd)_i$	0.511403	0.511406	0.511420	0.511371	0.511410
$\epsilon_{Nd}(t)$	−13.72	−13.67	−13.40	−14.36	−13.59
T_{DM1} (Ga)	2325	2331	2408	2428	2473
T_{DM2} (Ga)	2268	2264	2242	2319	2257
$^{208}Pb/^{204}Pb$	37.880	38.074	37.999	37.938	38.058
$^{207}Pb/^{204}Pb$	15.334	15.371	15.385	15.359	15.429
$^{206}Pb/^{204}Pb$	16.866	17.073	17.117	17.007	17.272
$(^{206}Pb/^{204}Pb)_i$	16.811	16.961	17.029	16.907	17.157
$(^{207}Pb/^{204}Pb)_i$	15.331	15.365	15.380	15.353	15.422
$(^{208}Pb/^{204}Pb)_i$	37.768	37.895	37.845	37.805	37.870

$\lambda_{Rb} = 1.42 \times 10^{-11}$ a^{-1}, $\lambda_{Sm} = 6.54 \times 10^{-12}$ a^{-1} (Lugmair & Marti, 1978); $(^{147}Sm/^{144}Nd)_{CHUR} = 0.1967$ (Jacobsen & Wasserburg, 1980); $(^{143}Nd/^{144}Nd)_{CHUR} = 0.512638$ (Goldstein *et al.* 1984); $(^{143}Nd/^{144}Nd)_{DM} = 0.513151$, $(^{147}Sm/^{144}Nd)_{DM} = 0.2136$ (Liew & Hofmann, 1988).
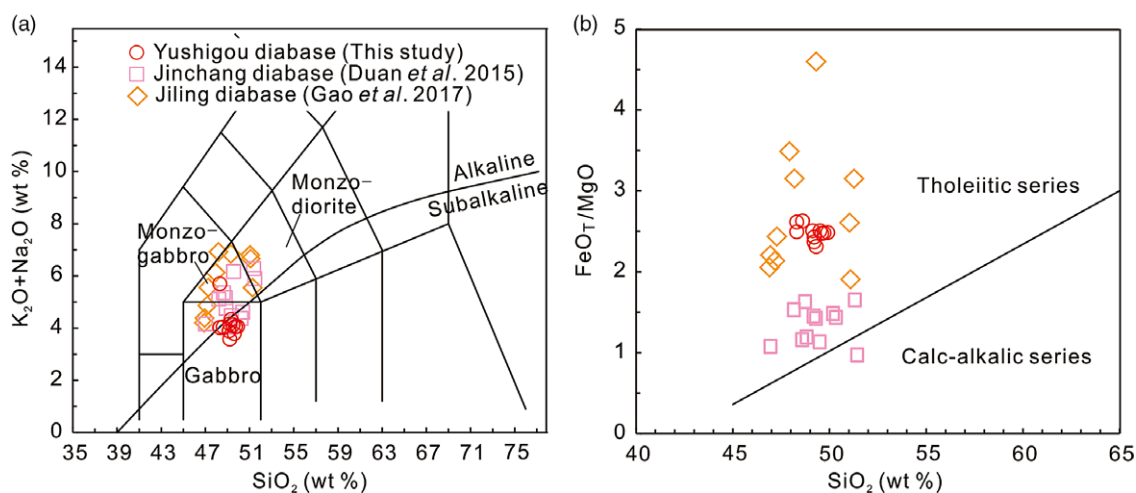
Fig. 4. (Colour online) (a) Total alkali versus silica diagram (after Middlemost, 1994). (b) FeO$_T$/MgO versus SiO$_2$ diagram (after Miyashiro, 1974).

basement is dated at 1724 ± 19 Ma (Tung *et al.* 2007). Moreover, there are no late Silurian intermediate–acid igneous rocks in the Jinchang mining area, and the *c.* 416 Ma Jilin granitic pluton occurs at *c.* 33 km SW of the Yushigou diabase. These *c.* 414 Ma zircons are therefore not likely the inherited zircons from the surrounding rock. The weighted mean $^{206}Pb/^{238}U$ age of 414 ± 9 Ma (MSWD = 0.47) is taken to represent the crystallization age of the Yushigou diabase.

6.b. Petrogenesis

Magmatic evolution, such as wall-rock assimilation or contamination, magma mixing and fractional crystallization, can exert important effects on the compositional and isotopic variations. Prior to exploring the nature of its mantle sources, the possible influence of magmatic evolution in the Yushigou diabase is evaluated below (Allen *et al.* 2013).
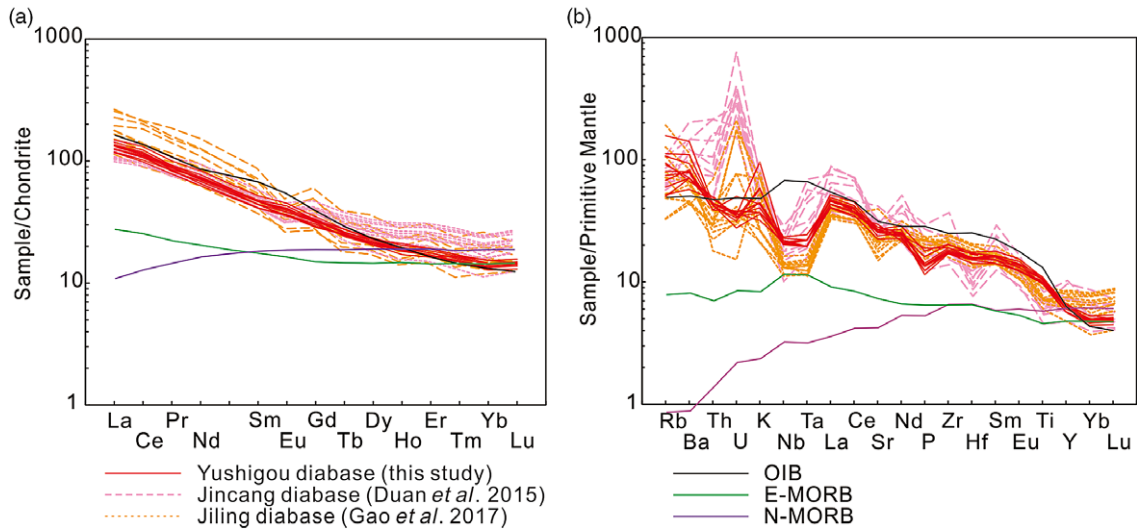
Fig. 5. (Colour online) (a) Chondrite-normalized REE patterns. (b) Primitive mantle-normalized trace-element patterns. Chondrite, primitive mantle, OIB (oceanic island basalt), N-MORB (N-type mid-ocean ridge basalt) and E-MORB (E-type mid-ocean ridge basalt) values are from Sun & McDonough (1989).
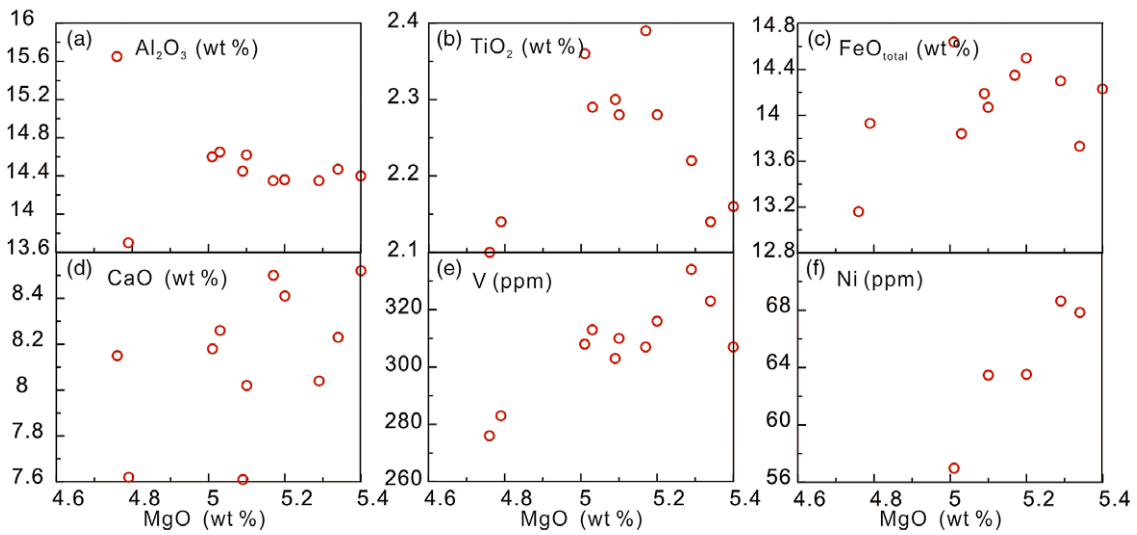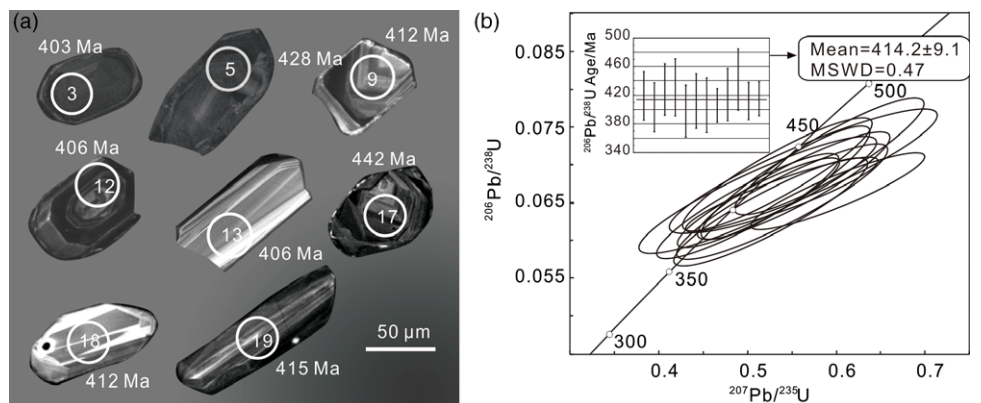

Fig. 6. (Colour online) (a–f) Harker diagrams.

Fig. 7. (Colour online) (a) CL images of zircons. (b) Concordia diagrams for zircon LA-ICP-MS U–Pb analyses. Numbers in the circles are the spot numbers. Numbers near the analytical spots are the U–Pb ages (Ma).
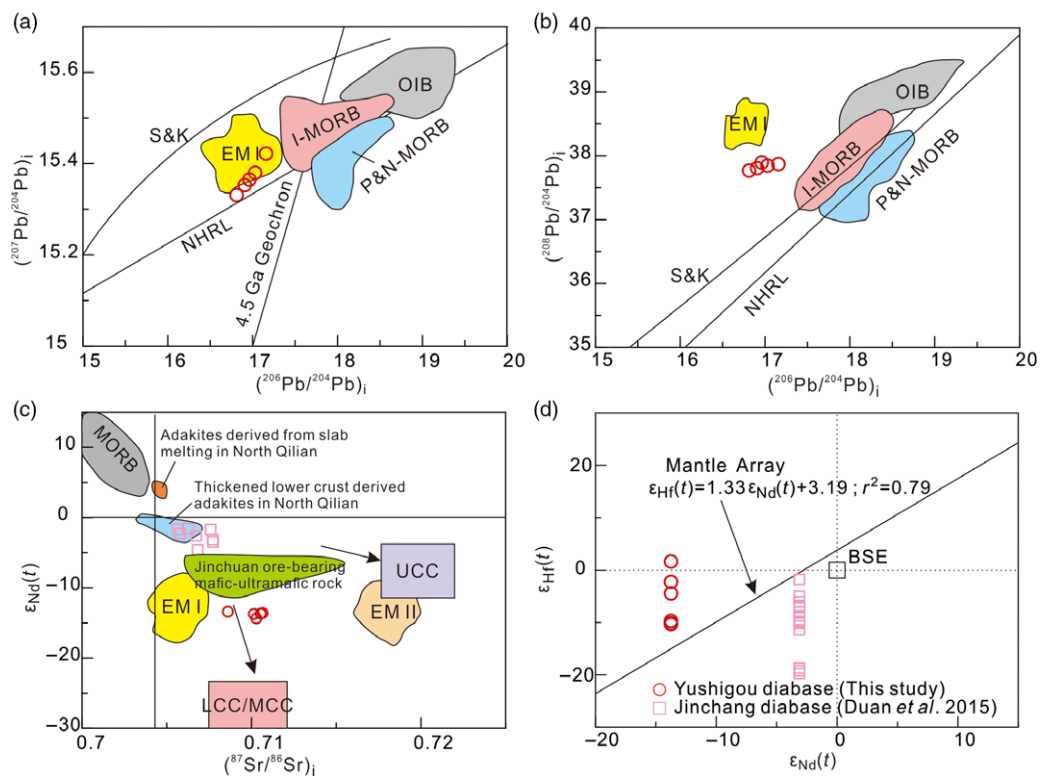
Fig. 8. (Colour online) (a) $(^{207}Pb/^{204}Pb)_i$ versus $(^{206}Pb/^{204}Pb)_i$ diagram. (b) $(^{208}Pb/^{204}Pb)_i$ versus $(^{206}Pb/^{204}Pb)_i$ diagram. (c) $\epsilon_{Nd}(t)$ versus $(^{87}Sr/^{86}Sr)_i$ diagram. (d) $\epsilon_{Nd}(t)$ versus $\epsilon_{Hf}(t)$ diagram (after Vervoort *et al.* 1999). Data sources include I-MORB (Indian mid-ocean ridge basalt), P&N-MORB (Pacific and North Atlantic mid-ocean ridge basalt), EM-I (enriched mantle type-I) and EM-II (enriched mantle type-II) as well as NHRL (Northern Hemisphere reference line) and 4.55 Ga geochron from Barry & Kent (1998), Zou *et al.* (2000), Hart (1984) and Zindler & Hart (1986). S&K (crustal lead evolution) is from Stacey & Kramers (1975). LCC (lower continental crust), MCC (middle continental crust) and UCC (upper continental crust) are from Jahn *et al.* (1999). Jinchuan ore-bearing mafic–ultramafic rock data are from Zhang *et al.* (2004), Duan *et al.* (2016) and Tang *et al.* (2018). Adakites derived from slab melting and from thickened lower crust in North Qilian are from Zhang *et al.* (2017b).
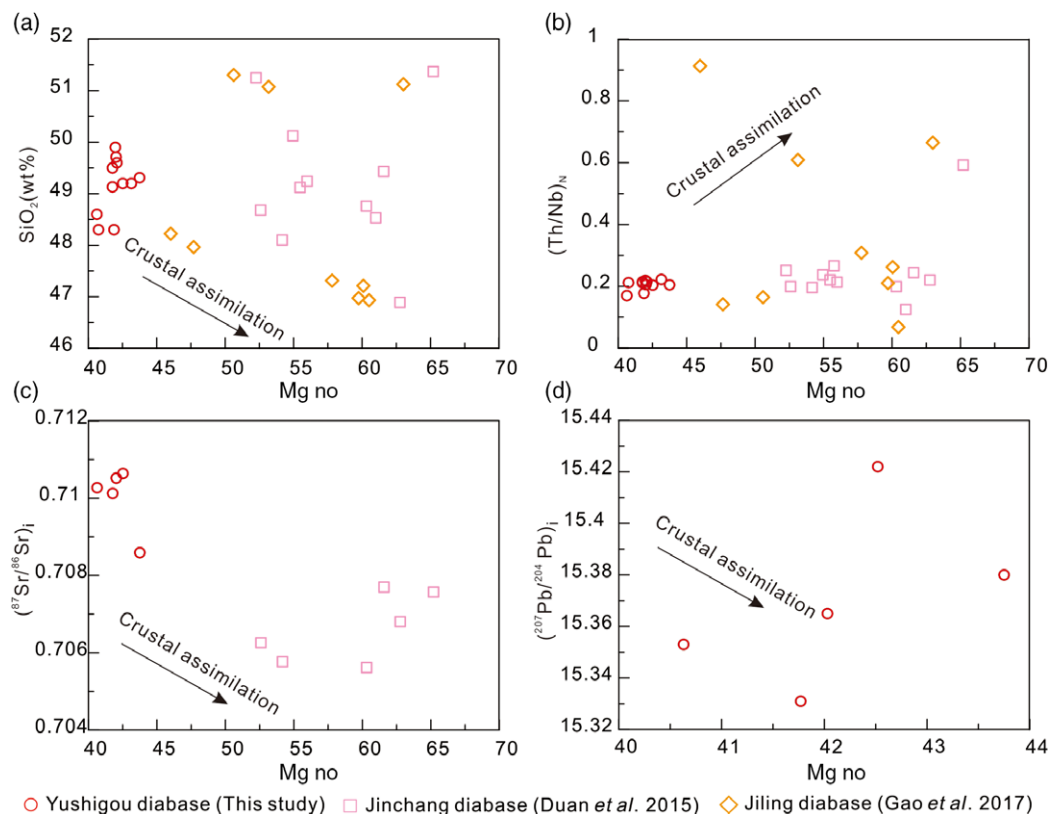

Fig. 9. (Colour online) (a) SiO_2 versus Mg no. diagram. (b) $(Th/Nb)_N$ versus Mg no. diagram. (c) $(^{87}Sr/^{86}Sr)_i$ versus Mg no. diagram. (c) $(^{207}Pb/^{204}Pb)_i$ versus Mg no. diagram.

6.b.1. Crustal contamination

Contamination by crustal materials will generally result in an increase in SiO_2 content and a decrease in MgO content. The Yushigou diabase samples have low and uniform SiO_2 contents (48.30–49.90 wt%), and there are no correlations between SiO_2 and Mg no. (Fig. 9a), which is inconsistent with the results of crustal contamination. Moreover, the Yushigou diabase has higher FeO_{total} (13.16–14.64 wt%), Ba (401–986 ppm) and Sr

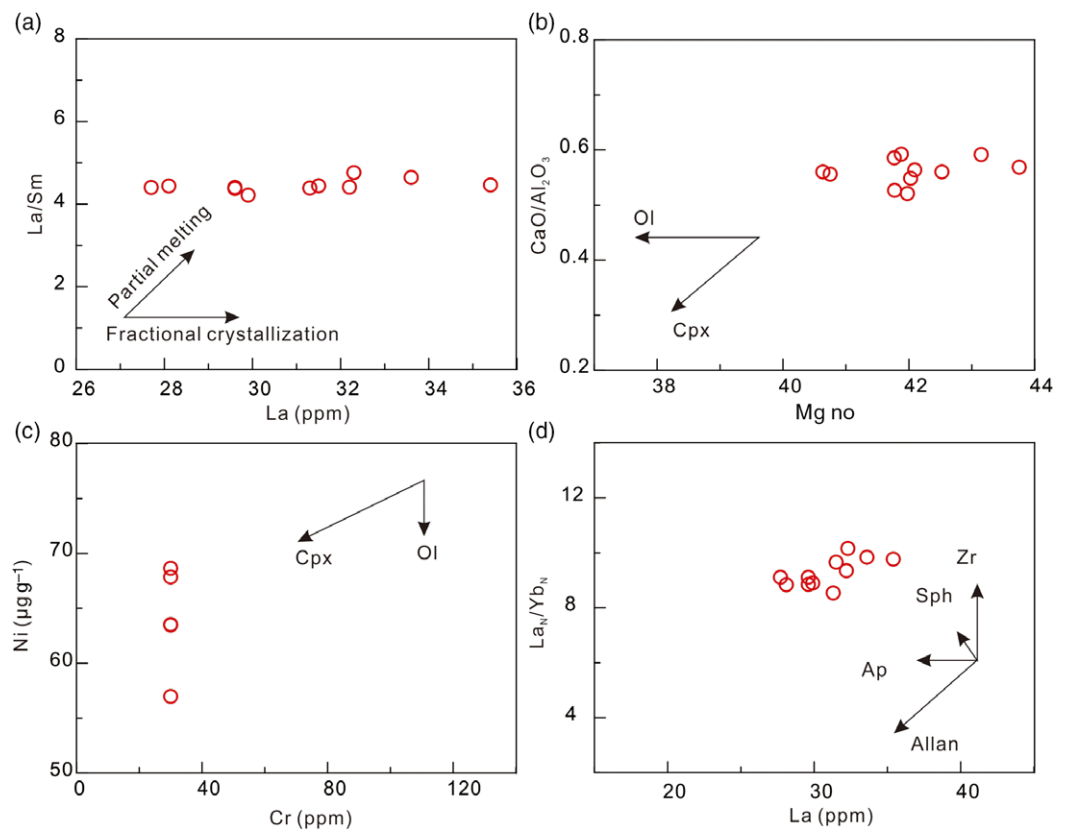**Fig. 10.** (Colour online) (a) La/Sm versus La diagram (after Treuil & Joron, 1975). (b) CaO/Al$_2$O$_3$ versus Mg no. diagram. (c) Ni versus Cr diagram. (d) La$_N$/Yb$_N$ versus La diagram.

(473–626 ppm) contents than the average continental crust (FeO$_{total}$ = 6.71 wt%, Rudnick & Shan, 2003; Ba = 390 ppm, Sr = 325 ppm, Rudnick & Fountain, 1995), which is an unfavourable effect of significant crustal contamination. Furthermore, the diabase has a weak variation in trace elements and no negative anomalies of Eu and Ti (Fig. 5). There are no linear correlations between Mg no. value and (Th/Nb)$_N$ ratio (Fig. 9b). The above features imply that the major and trace elements were not obviously affected by crustal contamination (Rudnick & Fountain, 1995; Ma *et al.* 2014; Wang *et al.* 2016). In addition, the samples of the Yushigou diabase have relatively uniform $\epsilon_{Nd}(t)$ values (−14.4 to −13.4). Although (^{87}Sr/^{86}Sr)$_i$ and (^{207}Pb/^{204}Pb)$_i$ have a relatively large range of variation, the crustal contamination trend is absent from the (^{87}Sr/^{86}Sr)$_i$ versus Mg no. diagram and (^{207}Pb/^{204}Pb)$_i$ versus Mg no. diagram (Fig. 9c, d). The combined evidence therefore indicates that the Yushigou diabase encountered negligible crustal contamination during their ascent.

6.b.2. Fractional crystallization

As shown in the La/Sm versus La diagram (Fig. 10a), increasing La content with constant La/Sm shows that fractional crystallization is the main factor controlling the composition of the Yushigou diabase. Compared with the primitive mantle magmas, the low MgO (4.76–5.40 wt%), Ni (56.98–68.64 ppm) and Cr (30–40 ppm) contents and Mg no. value (41–44) of the Yushigou diabase imply that fractional crystallization of mafic minerals, such as olivine and pyroxene, occurred prior to its emplacement (Frey & Prinz, 1978; Wang *et al.* 2016). This result is consistent with the positive correlation of MgO content with FeO$_{total}$, V and Ni contents (Fig. 6). The increasing Mg no. value and Ni content with nearly constant CaO/Al$_2$O$_3$ ratio and Cr content indicate that olivine is likely dominating the fractional phase (Fig. 10b, c). The increasing

La content with constant (La/Yb)$_N$ ratio (Fig. 10d), along with the clear P anomalies in the primitive-mantle-normalized trace-element diagrams (Fig. 5b), implies the fractionation of apatite (Wang *et al.* 2016). The plagioclase fractionation is precluded by the absence of the Eu anomaly (Fig. 5). Accordingly, the compositional characteristics of the Yushigou diabase are consistent with olivine and apatite fractionation.

6.b.3. Source characteristics

The Yushigou diabase is characterized by a relatively low $\epsilon_{Nd}(t)$ value (−14.4 to −13.4), EM-I-like Pb isotopic compositions, an enrichment in alkali, LREE and LILE contents, and a depletion in HFSE and HREE contents. These results indicate that the rock was derived from an enriched mantle source and/or it underwent extensive crustal contamination during ascent within the continental crust (Li *et al.* 2015; Zeng *et al.* 2018). As mentioned in Section 6.b.1, the Yushigou diabase did not undergo substantial crustal contamination during magmatic evolution. The geochemical and isotopic features of the Yushigou diabase were therefore mainly inherited from their EM-I-type magma source, rather than from a MORB- or ocean-island-basalt (OIB) -type asthenospheric mantle source.

The Yushigou diabase shows a depletion in HFSE content, negative Nb–Ta anomalies and high La/Nb ratios (> 1) (Fig. 5b), a characteristic of a subduction process (Zeng *et al.* 2018). Furthermore, compared with normalized (N-) MORB, the samples of the diabase have a higher Th/Yb ratio (Fig. 11a), indicating the addition of Th from the downgoing slab in the mantle source (Li & Chen, 2014). During subduction processes, slab-derived fluids and sediment-derived silicic or carbonatite melts can change the chemical composition of the mantle wedge (Menzies, 1987). The samples of diabase have (Hf/Sm)$_N$ and (Ta/La)$_N$ ratios of 0.95–1.07 and 0.40–0.53, respectively, and plot in or near the
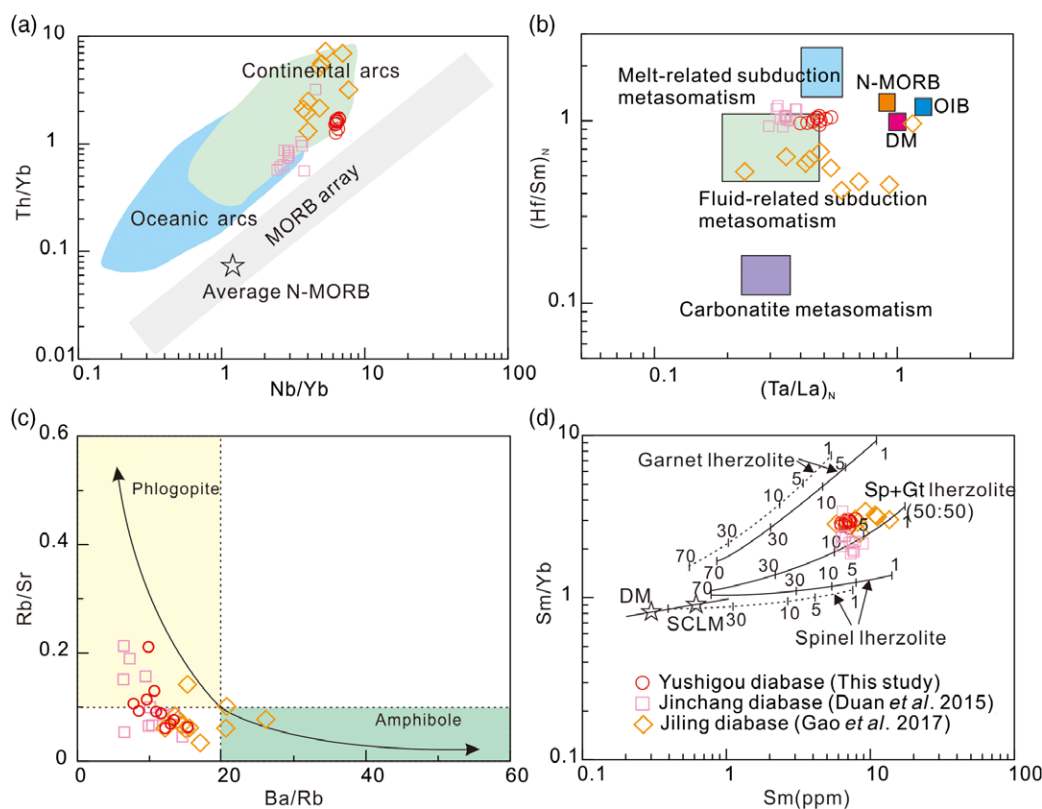
Fig. 11. (Colour online) (a) Th/Yb versus Nb/Yb diagram (after Pearce & Peate, 1995). (b) $(Hf/Sm)_N$ versus $(Ta/La)_N$ diagram (after LaFlèche *et al.* 1998). (c) Rb/Sr versus Ba/Rb diagram. (d) Sm/Yb versus Sm diagram. Modelling results of mantle melting with different starting materials (garnet lherzolite, garnet-spinel lherzolite and spinel lherzolite) are shown, based on the non-batch melting equations of Shaw (1970). The dashed and solid lines are the melting trends for depleted mantle (DM, $Sm = 0.3$ ppm and $Sm/Yb = 0.86$, McKenzie & O'Nions, 1991) and enriched subcontinental lithospheric mantle (SCLM, $Sm = 0.6$ ppm and $Sm/Yb = 0.96$, Aldanmaz *et al.* 2000), respectively. Partition coefficients used in the modelling are from McKenzie & O'Nions (1991). The numbers beside the lines are degrees of partial melting for a given mantle source. Average N-MORB (normal-MORB) value is after Sun & McDonough (1989).

fluid-related field (Fig. 11b), indicating that slab-derived fluids acted as the predominant metasomatic agent (LaFlèche *et al.* 1998). We therefore suggest that the enriched mantle source of the Yushigou diabase experienced metasomatism by fluids released from the subduction slab.

The high K_2O contents and significant enrichments in LILEs and LREEs in the Yushigou diabase require the presence of volatile-bearing minerals such as phlogopite and amphibole in the mantle source (Foley *et al.* 1996). Melts of an amphibole-bearing source have lower Rb/Sr ratio (< 0.1) and higher Ba/Rb ratio (> 20), while melts in equilibrium with phlogopite have higher Rb/Sr ratio (> 0.1) and lower Ba/Rb ratio (< 20) (Furman & Graham, 1999; Ma *et al.* 2014). The Yushigou diabase shows a wide range of Rb/Sr (0.06–0.21) and lower Ba/Rb (7.81–15.47) ratios (Fig. 11c), implying that amphibole and phlogopite might coexist in its mantle source area.

Since Sm is significantly affected by variation in the source mineralogy (e.g. garnet or spinel), whereas Yb is compatible with garnet but not with clinopyroxene or spinel, the two incompatible elements can be used to determine the mantle source mineralogy (Li & Chen, 2014). As shown in the Sm/Yb versus Sm diagram (Fig. 11d), all samples of the Yushigou diabase plot between the partial melting curves of garnet lherzolite and spinel+garnet facies (1:1) lherzolite. Garnet and spinel therefore coexist in the mantle source area of the Yushigou diabase. This view is further reinforced by the Dy/Yb ratios (2.19–2.41) of the Yushigou diabase, which is between the spinel stability field (Dy/Yb > 2.5) and the garnet stability field (Dy/Yb < 1.5) (Ma *et al.* 2014). It is generally considered that the depth of the garnet–spinel stability zone is between 75 and 85 km in the upper mantle (McKenzie & O'Nions, 1991). The Yushigou diabase was therefore likely formed in the spinel–garnet transition zone at a depth of 75–85 km.

6.c. Implication for the lithospheric mantle beneath the Longshoushan area

In the Longshoushan area, there are two other early Palaeozoic mantle-derived magmas: the 485 Ma Jiling diabase (Gao *et al.* 2017) and the 424–421 Ma Jinchang diabase (Duan *et al.* 2015). As shown in Figure 9, there are no linear correlations between Mg no. value and either SiO_2 contents, $(Th/Nb)_N$ ratios, $(^{87}Sr/^{86}Sr)_i$ or $(^{207}Pb/^{204}Pb)_i$, indicating that the parental magmas of two diabase dykes most likely experienced negligible crustal contamination during their ascent. Their geochemical composition can therefore be used to reflect the nature of the mantle source. The Jinchang diabase and the Jiling diabase have similar geochemical compositions to the Yushigou diabase, such as the enrichment in LREE and LILE, the depletion in HREE, Nb and Ta (Fig. 5), Dy/Yb ratios of 1.89–2.42, and the enriched Nd and Hf isotopic compositions (Fig. 8d). Moreover, as shown in Figure 11, the samples of the two diabase dykes fall within the same fields as those of the Yushigou diabase. Similar to the Yushigou diabase, the Jinchang diabase and the Jiling diabase were derived from partial melting of the enriched mantle source in the spinel–garnet transition zone, which was previously metasomatized by the slab-derived fluids. Nd model ages for the Jinchang diabase range between 1385 and 1620 Ma, suggesting that Sm/Nd fractionation in the lithospheric mantle from which these dyke magmas were derived began after 1620 Ma (Goodenough *et al.* 2002). The main tectonic event in the region, before the North Qilian orogeny, was the 1950–1800 Ma orogeny (Zeng *et al.* 2018). The enrichment of the mantle source was therefore most likely related to the North Qilian orogeny. We therefore suggest that the spinel–garnet transition zone in the lithospheric mantle beneath the Longshoushan area experienced metasomatism by fluids released from the subduction slab during the North Qilian orogeny.

Since the Lu–Hf and Sm–Nd isotopic systems have similar geochemical characteristics, the $\epsilon_{Hf}(t)$ and $\epsilon_{Nd}(t)$ values are commonly correlated (Vervoort *et al.* 1999). However, the values of the Yushigou diabase and Jinchang diabase significantly deviate from the mantle array ($\epsilon_{Hf}(t) = 1.33 \times \epsilon_{Nd}(t) + 3.19$, Vervoort *et al.* 1999) (Fig. 8d). Meanwhile, the two diabase dykes have different Nd–Hf decoupling types, and the $\epsilon_{Nd}(t)$ values of the Jinchang diabase are obviously higher than those of the Yushigou diabase (Fig. 8d).

The Nd–Hf decoupling of magmatic rocks is usually related to the garnet effect and the zircon effect (Patchett *et al.* 1982, 2004; Vervoort & Blichert-Toft, 1999; Vervoort *et al.* 2000; Wang *et al.* 2015). The garnet effect involves the presence of garnet residue during partial melting of mantle. Since the partition coefficients of Lu, Hf, Sm and Nd between garnet and melt are Lu > Sm > Nd > Hf, garnet residue surviving from a melting event will mean that the decrease of the Lu/Hf ratio in the magma is greater than that of the Sm/Nd ratio. This means that the magma will have a slower Hf evolution than that of Nd and, with time, will diverge from the mantle array with increasingly negative $\epsilon_{Hf}(t)$ values (Vervoort *et al.* 1999). On the other hand, since Hf^{4+} and Zr^{4+} have similar ionic radii, Hf can exist in the zircon in form of isomorphism. Zircon therefore has a high Hf value and extremely low Lu/Hf ratio (much lower than most other rock-forming minerals) (Vervoort *et al.* 2011). Over time this results in lower $\epsilon_{Hf}(t)$ value of zircon than that of other minerals. The $\epsilon_{Hf}(t)$ value of zircon-rich sediments/rocks is therefore relatively low and that of zircon-free sediments/rocks is relatively high (Patchett *et al.* 1984; Carpentier *et al.* 2009), while the Sm–Nd isotopic system is not affected by zircon since Sm/Nd ratios of zircons and bulk rock are similar. This striking feature is referred to as the 'zircon free'. In addition, Nd is more soluble than Hf in both aqueous fluids and siliceous melts, especially in the aqueous fluids (Pearce *et al.* 1999; Polat & Münker, 2004). The lithospheric mantle metasomatized by subduction-derived fluids and/or melts would therefore be expected to result in deviations from the mantle array on the $\epsilon_{Hf}(t)$–$\epsilon_{Nd}(t)$ isotope projection.

The zircon $\epsilon_{Hf}(t)$ value of the Jinchang diabase deviates negatively from its whole-rock $\epsilon_{Nd}(t)$ value with reference to the mantle array (Fig. 8d). Due to the low zircon content in mantle source, the Nd–Hf isotopic decoupling of the Jinchang diabase should not be related to the existence of a large amount of ancient zircon in the source area. As mentioned before, the Jinchang diabase is derived from a garnet–spinel transition region. The Nd–Hf decoupling of the Jinchang diabase is therefore most likely controlled by the residual garnet in the source area. Meanwhile, the Jinchang diabase, which has not experienced significant crustal contamination but has a variable $\epsilon_{Hf}(t)$ value, is most likely related to the inhomogeneity of garnet residue surviving in the source area from the melting event. The Yushigou diabase has significantly lower $\epsilon_{Nd}(t)$ value than that of the Jinchang diabase, indicating a higher metasomatism degree of subducted materials in its mantle source. This is consistent with the feature in the $(^{87}Sr/^{86}Sr)_i$–$\epsilon_{Nd}(t)$ diagram showing that the samples of the Yushigou diabase drop further to the MORB area than that of the Jinchang diabase (Fig. 8c). The Yushigou diabase has no negative Eu anomalies, which are different from the characteristics of oceanic gabbros (Sobolev *et al.* 2000). Moreover, as shown in Figure 8c, the $\epsilon_{Nd}(t)$ values (−14.4 to −13.4) of the Yushigou diabase are much lower than those of the Qilian adakites, which were derived from partial melting of the North Qilian oceanic crust. Ancient continental

materials from the subduction slab therefore seem to be a better candidate for the source of recycled materials in the mantle source. The $\epsilon_{Hf}(t)$ values of the Yushigou diabase are obviously higher than its $\epsilon_{Nd}(t)$ value, indicating that the recycled materials should be derived from zircon-free sediments or rocks such as mud, shale and pelagic sediment. This is consistent with the fact that the Nd/Zr ratios of Yushigou diabase are significantly higher than those of the primitive mantle ($Nd_N/Zr_N = 1.22–1.47$). Similar to the Jinchang diabase, the Yushigou diabase is likely to be affected by the garnet residue surviving in the source area, causing the variable $\epsilon_{Hf}(t)$ value. However, the recycled low zircon-free sediments or rocks in the source area is the main factor that determines the Nd–Hf decoupling type of the Yushigou diabase.

Two possible mechanisms can be considered for the different Nd–Hf decoupling types of the two diabase dykes. One is that the lithospheric mantle in the Longshoushan area is not uniformly metasomatized by the subducted slab. Another possibility is that the lithospheric mantle in the Longshoushan area was strongly metasomatized during the period from the formation of the Jinchang diabase (424 Ma) to the formation of the Yushigou diabase (414 Ma). As mentioned above, the Yushigou diabase and the Jinchang diabase are exposed in the same area, and have the same nature of mantle source, indicating that the two are likely derived from almost the same lithospheric mantle region. Because the incompatible elements (e.g. Th and U) tend to be enriched in the silicate melt during partial melting process, magmatic activity will lead to the depletion of Th and U in the source area. The younger Yushigou diabase therefore has significantly lower Th and U contents than those of the older Jinchang diabase, which also implies that these two diabases were likely generated from the same magmatic source. Hence, the second mechanism is most likely the reason for the different Nd–Hf decoupling types between the two diabase dykes, although more work is needed to verify this conclusion.

6.d. Tectonic implication

LA-ICP-MS zircon U–Pb data constrain the emplacement age of the Yushigou diabase and the Jinchang diabase at 414 Ma and 424–421 Ma, respectively, which obviously occur later than the closure of the North Qilian Ocean during Late Ordovician time (Song *et al.* 2013; Yu *et al.* 2015; Xia *et al.* 2016; Zeng *et al.* 2016; Sun *et al.* 2017; Zhang *et al.* 2017b). In addition, the samples of the Yushigou diabase have high Th/Nb (0.52–0.66) and Nb/Zr (0.057–0.061) ratios, and the samples of the Jinchang diabase have high Th/Nb (0.15–0.71) and Nb/Zr (0.035–0.046, average value = 0.041) ratios, which are similar to intraplate basalt ratios (Th/Nb > 0.11 and Nb/Zr > 0.04; Sun *et al.* 2007). Moreover, in the Zr/Y versus Zr diagram and 2Nb – (Zr/4) – Y diagram, the samples of the Yushigou diabase and the Jinchang diabase both fall in the within-plate basalt field (Fig. 12). In addition, Zeng *et al.* (2016) and Zhang *et al.* (2017b) reported that the Silurian A-type granites in the Longshoushan area were formed in the intraplate-extensional postcollisional setting. The Yushigou and Jinchang diabase in the Longshoushan area was therefore most likely formed in the intraplate environment after the closure of the North Qilian Ocean.

There are two different views about the mechanism for the postcollisional magmatism in the NQOB: the slab break-off (Song *et al.* 2009; Xiong *et al.* 2012; Xia *et al.* 2016; Huang *et al.* 2018); and lithospheric delamination (Wu *et al.* 2010; Yu *et al.* 2015; Zhang *et al.* 2017b). As mentioned above (Section 6.c), the Yushigou diabase and the Jinchang diabase are derived from the enriched
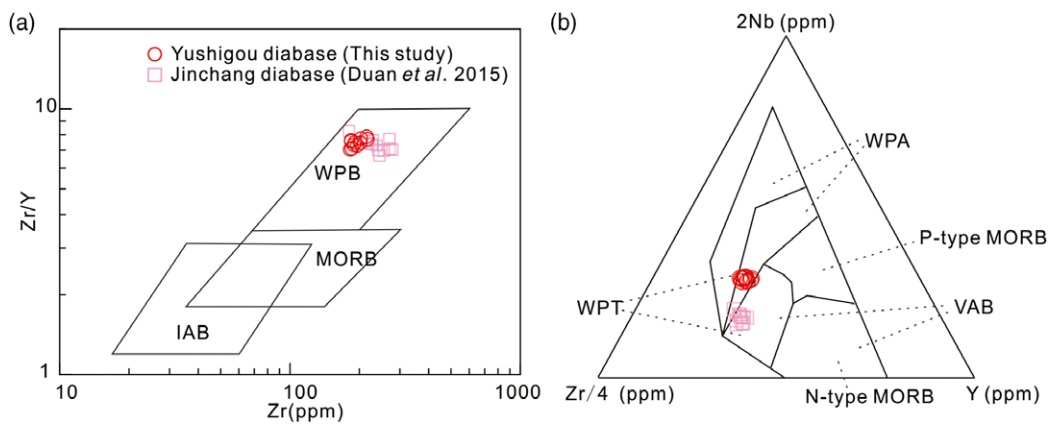
Fig. 12. (Colour online) (a) Zr/Y versus Zr diagram (after Pearce, 1982). (b) 2Nb – (Zr/4) – Y diagram (after Meschede, 1986). WPB – within-plate basalt; MORB – mid-ocean ridge basalt; IAB – island-arc basalt; WPA – within-plate alkali basalts; WPT – within-plate tholeiites; VAB – volcanic-arc basalts.
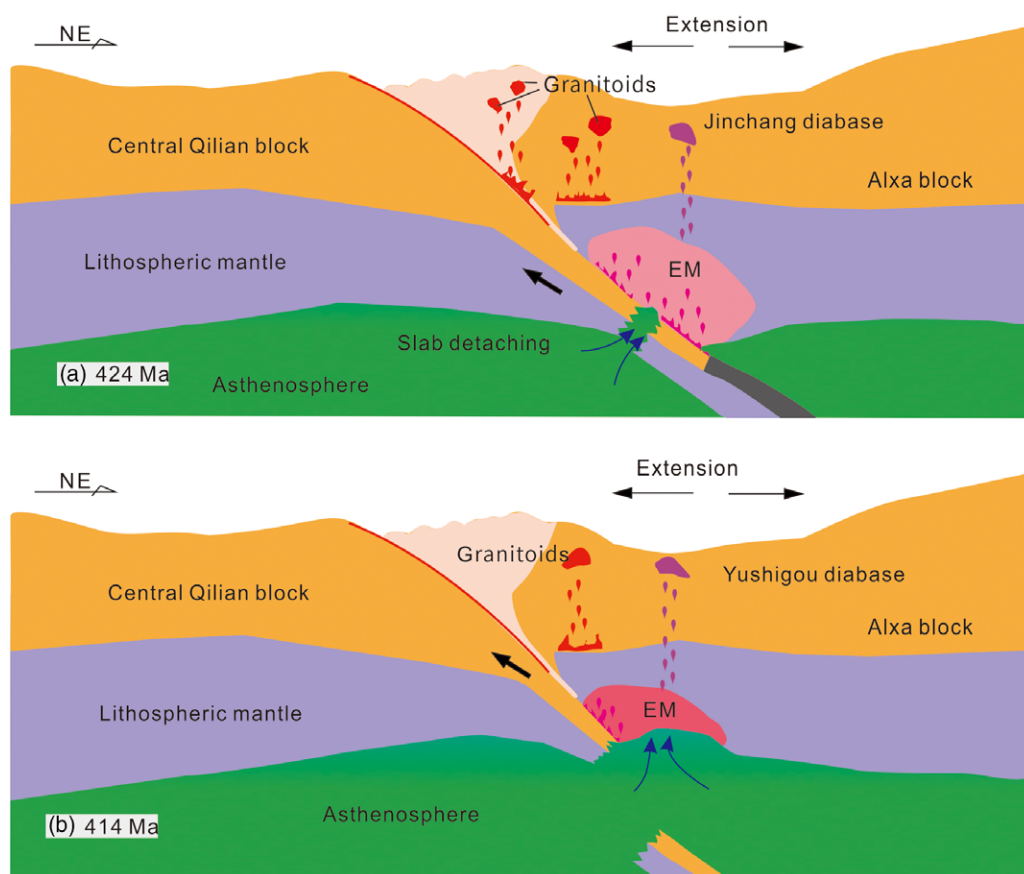

Fig. 13. (Colour online) Tectonic evolution of the NQOB in two phases during the middle–late Silurian period.

lithospheric mantle. This is different from the mafic magma formed under the tectonic background of lithospheric delamination, which has generally depleted radiogenic isotopic signatures (Wang *et al.* 2014; Song *et al.* 2015). In addition, the Ar–Ar ages of 423–411 Ma and zircon retrograde metamorphic ages of 424–404 Ma from North Qilian high-pressure–low-temperature (HP-LT) metamorphic rocks are considered to represent the age of greenschist facies overprinting during the exhumation (Zhang *et al.* 2007; Song *et al.* 2009, 2013; Li *et al.* 2010; Xia *et al.* 2016). During continental exhumation, the mantle peridotite of the overlying lithospheric mantle would be intensively metasomatized by hydrous melts or supercritical fluids released from the slab, as a result of the significant differences in compositions between the deep subducted continental crust and the overlying

mantle (Xiao *et al.* 2015; Zheng *et al.* 2015). This is consistent with the fact that the mantle source of the Yushigou diabase experienced strongly metasomatism by fluids released from the subduction slab, as mentioned above (Section 6.c). We therefore propose to use the slab break-off model to explain the post-collisional magmatism in the Longshoushan area during the middle–late Silurian period (Fig. 13).

During the exhumation of the subducted continental crust, the zircon-free sediments or rocks on the continental crust underwent strong dehydration and melting, which metasomatized the overlying lithospheric mantle beneath the Longshoushan area. This resulted in a strong enrichment of Nd isotopes in the lithospheric mantle of the Longshoushan area. Subsequently, hot asthenospheric mantle upwelling occurred near the break-off point, which

provides the thermal flux to melt the overlying lithospheric mantle and the lower continental crust. A series of post-collisional acid and mafic magmatic rocks therefore formed in the Silurian period.

7. Conclusion

(1) LA-ICP-MS zircon U–Pb dating indicates that the Yushigou diabase in the Longshoushan area formed at 414 Ma.

(2) Geochemical and isotopic tracing suggests that the Yushigou diabase was derived from partial melting of an EM-I-type subcontinental lithospheric mantle, which was metasomatized by slab-derived fluids released from the subducted slab. During emplacement, the parental magma of the Yushigou diabase experienced fractionation of olivine and apatite.

(3) The different types of Nd–Hf isotope decoupling between the Yushigou diabase and the Jinchang diabase can be explained by the fact that the lithospheric mantle beneath the Longshoushan area experienced strong metasomatism by the zircon-free sediments or rocks on the exhumation of the continental crust during the middle–late Silurian period.

(4) The post-collisional magmatism of the NQOB in the Silurian period is associated with post-collision slab break-off.

References

Aldanmaz E, Pearce JA, Thirlwall MF and Mitchell JG (2000) Petrogenetic evolution of late Cenozoic, post-collision volcanism in western Anatolia, Turkey. *Journal of Volcanology and Geothermal Research* **102**, 67–95.

Allen MB, Kheirkhah M, Neill I, Emami MH and Mcleod CL (2013) Generation of arc and within-plate chemical signatures in collision zone magmatism: Quaternary lavas from Kurdistan Province, Iran. *Journal of Petrology* **54**, 887–911.

Barry TL and Kent RW (1998) Cenozoic magmatism in Mongolia and the origin of central and east Asian basalts. *Mantle Dynamics and Plate Interactions in East Asia* **27**, 347–64.

Blichert-Toft J and Albarède F (1997) The Lu-Hf isotope geochemistry of chondrites and the evolution of the mantle-crust system. *Earth and Planetary Science Letters* **148**, 243–58.

Carpentier M, Chauvel C, Maury RC and Mattielli N (2009) The "zircon effect" as recorded by the chemical and Hf isotopic compositions of Lesser Antilles forearc sediments. *Earth and Planetary Science Letters* **287**, 86–99.

Chen YX, Xia XH and Song SG (2012) Petrogenesis of Aoyougou high-silica adakite in the North Qilian orogen, NW China: evidence for decompression melting of oceanic slab. *Chinese Science Bulletin* **57**, 2289–301 (in Chinese with English abstract).

Cheng H, Lu TY and Cao DD (2016) Coupled Lu–Hf and Sm–Nd geochronology constrains blueschist-facies metamorphism and closure timing of the Qilian Ocean in the North Qilian orogen. *Gondwana Research* **34**, 99–108.

Duan J, Li CS, Qian ZZ and Jiao JG (2015) Geochronological and geochemical constraints on the petrogenesis and tectonic significance of Paleozoic dolerite dykes in the southern margin of Alxa Block, North China Craton. *Journal of Asian Earth Sciences* **111**, 244–53.

Duan J, Li CS, Qian ZZ, Jiao JG, Ripley EM and Feng YQ (2016) Multiple S isotopes, zircon Hf isotopes, whole-rock Sr-Nd isotopes, and spatial variations of PGE tenors in the Jinchuan Ni-Cu-PGE deposit, NW China. *Mineralium Deposita* **51**, 557–74.

Foley SF, Jackson SE, Fryer BJ, Greenouch JD and Jenner GA (1996) Trace element partition coefficients for clinopyroxene and phlogopite in an alkaline lamprophyre from Newfoundland by LAM-ICP-MS. *Geochimica et Cosmochimica Acta* **60**, 629–38.

Frey FA and Prinz M (1978) Ultramafic inclusions from San Carlos, Arizona: petrologic and geochemical data bearing on their petrogenesis. *Earth & Planetary Science Letters* **38**, 129–76.

Furman T and Graham D (1999) Erosion of lithospheric mantle beneath the East African Rift system: geochemical evidence from the Kivu volcanic province. *Developments in Geotectonics* **24**, 237–62.

Gao Y, Zhao RY, Wang G and Nie N (2017) Geochemical characteristics and geological implication of the Jiling diabase in Gansu province. *Geology and Resources* **26**, 505–14 (in Chinese with English abstract).

Goldstein SL, O'Nions RK and Hamilton PJ (1984) A Sm–Nd isotopic study of atmospheric dusts and particulates from major river systems. *Earth and Planetary Science Letters* **70**, 221–36.

Gong JH, Zhang JX, Wang ZQ, Yu SY, Li HK and Li YS (2016) Origin of the Alxa Block, western China: New evidence from zircon U–Pb geochronology and Hf isotopes of the Longshoushan Complex. *Gondwana Research* **36**, 359–75.

Goodenough KM, Upton BGJ and Ellam RM (2002) Long-term memory of subduction processes in the lithospheric mantle: evidence from the geochemistry of basic dykes in the Gardar Province of South Greenland. *Journal of the Geological Society* **159**, 705–14.

Gu HO, Xiao YL, Santosh M, Li WY, Yang XY, Pack A and Hou ZH (2013) Spatial and temporal distribution of Mesozoic adakitic rocks along the Tan-Lu fault, Eastern China: constraints on the initiation of lithospheric thinning. *Lithos* **177**, 352–65.

Hart RS (1984) A large-scale isotope anomaly in the Southern Hemisphere mantle. *Nature* **309**, 753–57.

Hu NG, Xu AD and Yang JX (2005) Characteristics and tectonic environment of Zhigoumen pluton in Longshoushan area. *Journal of Earth Science and Enivronmental* **27**, 5–11 (in Chinese with English abstract).

Huang ZB, Zheng JP, Li BH, Dong XY, Fu TY, Xu L and Gao KL (2018) U-Pb ages, Hf isotopic composition and geochemistry of alkaline complex from the Ganshaebo REE deposit in North Qilian Mountains, China. *Acta Geologica Sinica* **92**, 2420–36 (in Chinese with English abstract).

Jacobsen SB and Wasserburg GJ (1980) Sm–Nd isotopic evolution of chondrites. *Earth and Planetary Science Letters* **50**, 139–55.

Jahn BM, Wu FY, Lo CH and Tsai CH (1999) Crust–mantle interaction induced by deep subduction of the continental crust: geochemical and Sr–Nd isotopic evidence from post-collisional mafic–ultramafic intrusions of the northern Dabie complex, central China. *Chemical Geology* **157**, 119–46.

Jiao JG, Jin SF, Rui HC, Zhang GP, Ning QF and Shao LQ (2017) Petrology, geochemistry and chronology study of the Xiaokouzi Mafic-ultramafic intrusion in the eastern section of Longshou Mountains, Gansu. *Acta Geologica Sinica* **91**, 736–47 (in Chinese with English abstract).

LaFlèche MR, Camiré G and Jenner GA (1998) Geochemistry of post-Acadian, Carboniferous continental intraplate basalts from the Maritimes Basin, Magdalen Islands, Quebec, Canada. *Chemical Geology* **148**, 115–36.

Li B, Jiang SY, Zhang Q, Zhao HX and Zhao KD (2015) Cretaceous crust–mantle interaction and tectonic evolution of Cathaysia Block in South China: evidence from pulsed mafic rocks and related magmatism. *Tectonophysics* **661**, 136–55.

Li JF, Zhang ZC and Han BF (2010) Geochronology and geochemistry of Early Paleozoic granitic plutons from Subei and Shibaocheng areas, the western segment of Central Qilian and their geological implications. *Acta Petrologica Sinica* **26**, 2431–44 (in Chinese with English abstract).

Li XH, Su L, Song B and Liu DY (2004) SHRIMP U-Pb zircon age of the Jinchuan ultramafic intrusion and its geological significance. *Chinese Science Bulletin* **49**, 420–22.

Li Z and Chen B (2014) Geochronology and geochemistry of the Paleoproterozoic meta-basalts from the Jiao-Liao-Ji Belt, North China

Craton: implications for petrogenesis and tectonic setting. *Precambrian Research* **255**, 653–67.

Liew TC and Hofmann AW (1988) Precambrian crustal components, plutonic associations, plate environment of the Hercynian Fold Belt of central Europe: indications from a Nd and Sr isotopic study. *Contributions to Mineralogy and Petrology* **98**, 129–38.

Lin YH and Zhang LF (2012) Petrology and 40Ar/39Ar geochronology of the lawsonite-bearing blueschist and eclogite from the Qingshuigou blueschist belt in North Qilian Mountains in NW China and their tectonic implication. *Acta Geologica Sinica* **86**, 1503–1524 (in Chinese with English abstract).

Liu YJ, Neubauer F, Genser J, Takasu A and Handler R (2006) 40Ar/39Ar ages of blueschist facies pelitic schists from Qingshuigou in the Northern Qilian Mountains, western China. *Island Arc* **15**, 187–98.

Lugmair GW and Marti K (1978) Lunar initial 143Nd/144Nd: differential evolution of the lunar crust and mantle. *Earth and Planetary Science Letters* **39**, 349–57.

Ma L, Jiang SY, Hou ML, Dai BZ, Jiang YH, Yang T, Zhao KD, Pu W, Zhu ZY and Xu B (2014) Geochemistry of Early Cretaceous calc-alkaline lamprophyres in the Jiaodong Peninsula: implication for lithospheric evolution of the eastern North China Craton. *Gondwana Research* **25**, 859–72.

McKenzie D and O'Nions RK (1991) Partial melt distributions from inversion of rare earth element concentrations. *Journal of Petrology* **32**, 1021–91.

Meng E, Liu FL, Liu PH, Liu CH, Yang H, Wang F, Shi JR and Cai J (2014) Petrogenesis and tectonic significance of Paleoproterozoic meta-mafic rocks from central Liaodong Peninsula, northeast China: evidence from zircon U–Pb dating and in situ Lu–Hf isotopes, and whole-rock geochemistry. *Precambrian Research* **247**, 92–109.

Menzies MA, Rogers N, Tindle AG and Hawkesworth CJ (1987) Metasomatic and enrichment processes in lithospheric peridotites, an effect of asthenosphere-lithosphere interaction. In *Mantle Metasomatism* (ed. MA Menzies), pp. 313–61. London: Academic Press.

Meschede M (1986) A method of discriminating between different types of mid-ocean ridge basalts and continental tholeiites with the Nb-Zr-Y diagram. *Chemical Geology* **56**, 207–18.

Middlemost EA (1994) Naming materials in the magma/igneous rock system. *Earth-Science Reviews* **37**, 215–24.

Miyashiro A (1974) Volcanic rock series in island arcs and active continental margins. *American Journal of Science* **274**, 321–55.

Næraa T, Scherstén A, Rosing MT, Kemp AIS, Hoffmann JE, Kokfelt TF and Whitehouse MJ (2012) Hafnium isotope evidence for a transition in the dynamics of continental growth 3.2 Gyr ago. *Nature* **485**, 627–30.

Nie L, Zhao RY, Chen X, Feng B, Wang G and Li Y (2016) Characteristics of diorite from Jiling Pluton and its relationship with uranium metallogenic in Longshou Mountains, Gansu Province. *Geoscience* **30**, 760–9 (in Chinese with English abstract).

Patchett PJ, Kouvo O, Hedge CE and Tatsumoto M (1982) Evolution of continental crust and mantle heterogeneity: evidence from Hf isotopes. *Contributions to Mineralogy and Petrology* **78**, 279–97.

Patchett PJ, White WM, Feldmann H, Kielinczuk S and Hofmann AW (1984) Hafnium/rare earth element fractionation in the sedimentary system and crustal recycling into the Earth's mantle. *Earth and Planetary Science Letters* **69**, 365–78.

Patchett PJ, Vervoort JD, Soderlund U and Salters VJM (2004) Lu-Hf and Sm-Nd isotopic systematics in chondrites and their constraints on the Lu-Hf properties of the Earth. *Earth and Planetary Science Letters* **222**, 29–41.

Pearce JA (1982) Trace element characteristics of lavas from destructive plate boundaries. *Andesites* **8**, 525–48.

Pearce JA, Kempton PD, Nowell GM and Noble SR (1999) Hf-Nd element and isotope perspective on the nature and provenance of mantle and subduction components in Western Pacific Arc-Basin systems. *Journal of Petrology* **40**, 1579–611.

Pearce JA and Peate DW (1995) Tectonic implications of the composition of volcanic arc magmas. *Annual Review of Earth and Planetary Sciences* **23**, 251–85.

Polat A and Münker C (2004) Hf–Nd isotope evidence for contemporaneous subduction processes in the source of late Archean arc lavas from the Superior Province, Canada. *Chemical Geology* **213**, 403–29.

Qin HP (2012) Petrology of early Paleozoic granites and their relation to tectonic evolution of orogen in the North Qilian Orogenic Belt. PhD thesis, Chinese Academy of Geological Sciences. Published thesis (in Chinese with English abstract).

Rudnick RL and Fountain DM (1995) Nature and composition of the continental crust: a lower crustal perspective. *Reviews of Geophysics* **33**, 267–309.

Rudnick R and Shan G (2003) The role of lower crustal recycling in continent formation. *Geochmica et Cosmochimica Acta* **67**, 403.

Shaw DM (1970) Trace element fractionation during anatexis. *Geochimica et Cosmochimica Acta* **34**, 237–43.

Sobolev AV, Hofmann AW and Nikogosian IK (2000) Recycled oceanic crust observed in 'ghost plagioclase' within the source of Mauna Loa lavas. *Nature* **404**, 986–90.

Söderlund U, Patchett PJ, Vervoort JD and Isachsen CE (2004) The 176 Lu decay constant determined by Lu–Hf and U–Pb isotope systematics of Precambrian mafic intrusions. *Earth and Planetary Science Letters* **219**, 311–24.

Song SG, Niu YL, Su L and Xia XH (2013) Tectonics of the North Qilian orogen, NW China. *Gondwana Research* **23**, 1378–401.

Song SG, Niu YL, Zhang LF, Wei CJ, Liou JG and Su L (2009) Tectonic evolution of early Paleozoic HP metamorphic rocks in the North Qilian Mountains, NW China: new perspectives. *Journal of Asian Earth Sciences* **35**, 334–53 (in Chinese with English abstract).

Song SG, Wang MJ, Wang C and Niu YL (2015) Magmatism during continental collision, subduction, exhumation and mountain collapse in collisional orogenic belts and continental net growth: a perspective. *Science China Earth Sciences* **58**, 1284–304.

Song SG, Zhang LF, Niu YL, Song B, Zhang GB and Wang QJ (2004) Zircon U-Pb SHRIMP ages of eclogites from the North Qilian Mountains in NW China and their tectonic implication. *Chinese Science Bulletin* **49**, 848–52 (in Chinese with English abstract).

Stacey JT and Kramers JD (1975) Approximation of terrestrial lead isotope evolution by a two-stage model. *Earth and Planetary Science Letters* **26**, 207–21.

Sun BL, Qian Q and Zhang JX (2017) Zircon U-Pb geochronology, Hf-O isotopes, whole-rock geochemistry of the Dafosi and Jinfosi granite plutons, Gansu Province and geological implications. *Acta Petrologica Sinica* **33**, 3091–108 (in Chinese with English abstract).

Sun H, Xiao YL, Gao YJ, Lai JQ, Hou ZH and Wang YY (2013) Fluid and melt inclusions in the Mesozoic Fangcheng basalt from North China Craton: implications for magma evolution and fluid/melt-peridotite reaction. *Contributions to Mineralogy and Petrology* **165**, 885–901.

Sun SQ, Zhang CJ and Zhao SJ (2007) Identification of the tectonic settings for continental intraplate by trace elements. *Geotectonica et Metallogenia* **31**, 104–9 (in Chinese with English abstract).

Sun SS and McDonough WF (1989) Chemical and isotopic systematics of oceanic basalts: implications for mantle composition and processes. In *Magmatism in the Ocean Basins* (eds AD Saunders and MJ Norry), pp. 313–45. Geological Society of London, Special Publication no. 42.

Tang QY, Bao J, Dang YX, Ke S and Zhao Y (2018) Mg–Sr–Nd isotopic constraints on the genesis of the giant Jinchuan Ni–Cu–(PGE) sulfide deposit, NW China. *Earth and Planetary Science Letters* **502**, 221–30.

Treuil M and Joron JL (1975) Utilisation des elements hygromagmatophiles pour la simplification de la modélisation quantitative des processusMagmatiques: exemples de l'Afar et de la dorsale médio-atlantique. *Societa Italiana Mineralogia e Petrologia* **31**, 125–74.

Tung KA, Yang HY, Liu DY, Zhang JX, Tseng CY and Wan YS (2007) SHRIMP U-Pb geochronology of the detrital zircons from the Longshoushan Group and its tectonic significance. *Chinese Science Bulletin* **52**, 1414–25.

Vervoort JD and Blichert-Toft J (1999) Evolution of the depleted mantle: Hf isotope evidence from juvenile rocks through time. *Geochimica et Cosmochimica Acta* **6**, 533–56.

Vervoort JD, Patchett PJ, Albarede F, Blicherttoft J, Rudnick RL and Downes H (2000) Hf-Nd isotopic evolution of the lower crust. *Earth and Planetary Science Letters* **181**, 115–29.

Vervoort JD, Patchett PJ, Blichert-Toft J and Albarède F (1999) Relationships between Lu–Hf and Sm–Nd isotopic systems in the global sedimentary system. *Earth and Planetary Science Letters* **168**, 79–99.

Vervoort JD, Plank T and Prytulak J (2011) The Hf–Nd isotopic composition of marine sediments. *Geochimica et Cosmochimica Acta* **75**, 5903–26.

Wang CY, Zhang Q, Qian Q and Zhou M (2005) Geochemistry of the early paleozoic Baiyin Volcanic Rocks (NW China): implications for the tectonic evolution of the North Qilian Orogenic Belt. *The Journal of Geology* **113**, 83–94.

Wang KX, Yu CD, Yan J, Liu XD, Liu WH and Pan JY (2019) Petrogenesis of Early Silurian granitoids in the Longshoushan area and their implications for the extensional environment of the North Qilian Orogenic Belt, China. *Lithos* **342–343**, 152–74.

Wang L, Wang GH, Lei SB, Wang W, Qing M, Jia LQ, Chang CJ, Kang JK and Hou WR (2016) Geochronology, geochemistry and Sr–Nd–Pb–Hf isotopes of the Paleoproterozoic mafic dykes from the Wulashan area, North China Craton: Petrogenesis and geodynamic implications. *Precambrian Research* **286**, 306–24.

Wang MJ, Song SG, Niu YL and Su L (2014) Post-collisional magmatism: Consequences of UHPM terrane exhumation and orogen collapse, N. Qaidam UHPM belt, NW China. *Lithos* **210–211**, 181–98.

Wang N, Wu CL, Lei M and Chen HJ (2018) Petrogenesis and tectonic implications of the Early Paleozoic granites in the western segment of the North Qilian orogenic belt, China. *Lithos* **312–313**, 89–107.

Wang N, Wu CL, Lei M, Chen HJ, Li MZ and Zheng WH (2017) Geochronology and petrogenesis of granite in Shibaocheng area from the North Qilian orogenic belt. *Acta Petrologica Sinica* **33**, 3909–24 (in Chinese with English abstract).

Wang X, Griffin WL, Chen J, Huang PY and Li X (2011) U and Th contents and Th/U ratios of zircon in felsic and mafic magmatic rocks: improved zircon-melt distribution coefficients. *Acta Geologica Sinica-English Edition* **85**, 164–74.

Wang X, Huang XL, Ma JL, Zhong JW and Yang QJ (2015) Hf–Nd isotopes of the early Precambrian metamorphic complexes in the southern segment of the Trans-North China Orogen: implications for crustal evolution. *Geotectonica et Metallogenia* **39**, 1108–18 (in Chinese with English abstract).

Wei QQ, Hao LB, Lu JL, Zhao YY, Zhao XY and Shi HL (2013) LA-MC-ICP-MS zircon U–Pb dating of Hexipu granite and its geological implications. *Bulletin of Mineralogy, Petrology and Geochemistry* **32**, 729–35 (in Chinese with English abstract).

Woodhead JD and Hergt JM (2005) A preliminary appraisal of seven natural zircon reference materials for in situ Hf isotope determination. *Geostandards and Geoanalytical Research* **29**, 183–95.

Wu CL, Xu XY, Gao QM, Li XM, Lei M, Gao YH, Frost RB and Wooden JL (2010) Early Palaeozoic granitoid magmatism and tectonic evolution in North Qilian, NW China. *Acta Petrologica Sinica* **26**, 1027–44 (in Chinese with English abstract).

Wu CL, Yang JS, Yang HY, Wooden J, Shi RD, Chen SY and Zheng QG (2004) Dating of two types of granite from north Qilian, China. *Acta Petrologica Sinica* **20**, 425–32 (in Chinese with English abstract).

Xia LQ, Li XM, Yu JY and Wang GQ (2016) Mid-late Neoproterozoic to early Paleozoic volcanism and tectonic evolution of the Qilianshan, NW China. *GeoResJ* **9–12**, 1–41.

Xia XH, Song SG and Niu YL (2012) Tholeiite–Boninite terrane in the North Qilian suture zone: Implications for subduction initiation and back-arc basin development. *Chemical Geology* **328**, 259–77.

Xiao YL, Sun H, Gu HO, Huang J, Li WY and Liu L (2015) Fluid/melt in continental deep subduction zones: compositions and related geochemical fractionations. *Science China-Earth Sciences* **58**, 1457–76.

Xie CR, Xiao PX and Yang ZZ (2013) Progress in the studying of the Hanmushan Group in the Longshou mountains of Gansu province. *Journal of Stratigraphy* **37**, 54–7 (in Chinese with English abstract).

Xiong ZL, Zhang HF and Zhang J (2012) Petrogenesis and tectonic implications of the Maozangsi and Huangyanghe granitic intrusions in Lenglongling area, the eastern part of North Qilian Mountain, NW China. *Earth Science Frontiers* **19**, 214–27 (in Chinese with English abstract).

Xu AD and Jiang XD (2003) Characteristics and geological significance of the Dunzigou Group of the mesoproterozoic in the western edge of the North China platform. *Journal of Earth Science and Enivronmental* **25**, 27–31 (in Chinese with English abstract).

Xue S, Ling MX, Liu YL, Zhang H and Sun WD (2017) The genesis of early Carboniferous adakitic rocks at the southern margin of the Alxa Block, North China. *Lithos* **278–281**, 181–94.

Yu SY, Zhang JX, Qin HP, Sun DY, Zhao XL, Cong F and Li YS (2015) Petrogenesis of the early Paleozoic low-Mg and high-Mg adakitic rocks in the North Qilian orogenic belt, NW China: implications for transition from crustal thickening to extension thinning. *Journal of Asian Earth Sciences* **107**, 122–39.

Zeng RY, Lai JQ, Mao XC, Li B, Ju PJ and Tao SL (2016) Geochemistry, zircon U–Pb dating and Hf isotopies composition of Paleozoic granitoids in Jinchuan, NW China: constraints on their petrogenesis, source characteristics and tectonic implication. *Journal of Asian Earth Sciences* **121**, 20–33.

Zeng RY, Lai JQ, Mao XC, Li B, Zhang JD, Bayless R and Yang LZ (2018) Paleoproterozoic multiple Tectonothermal events in the Longshoushan Area, Western North China Craton and their geological implication: evidence from geochemistry, Zircon U–Pb geochronology and Hf Isotopes. *Minerals* **8**, 361.

Zhang JM, Zhao RY, Wang G and Nie L (2017a) The geological characteristics and significances of A-type porphyritic granite in the Jiling uranium deposit in the Longshou Mountains, Gansu Province. *Bulletin of Mineralogy Petrology and Geochemistry* **36**, 813–23 (in Chinese with English abstract).

Zhang JX, Meng FC and Wan YS (2007) A cold Early Palaeozoic subduction zone in the North Qilian Mountains, NW China: petrological and U–Pb geochronological constraints. *Journal of Metamorphic Geology* **25**, 285–304.

Zhang LQ, Zhang HF, Zhang SS, Xiong ZL, Luo BJ, He Y, Pan FB, Zhou XC, Xu WC and Liang G (2017b) Lithospheric delamination in post-collisional setting: Evidence from intrusive magmatism from the North Qilian orogen to southern margin of the Alxa block, NW China. *Lithos* **288**, 20–34.

Zhang MJ, Kamo SL, Li CS, Hu PQ and Ripley EM (2010) Precise U–Pb zircon–baddeleyite age of the Jinchuan sulfide ore-bearing ultramafic intrusion, western China. *Mineralium Deposita* **45**, 3–9.

Zhang ZQ, Du AD, Tang SH, Lu J, Wang J and Yang G (2004) Age of the Jinchuan copper-nickel deposit and isotopic geochemical feature of its source. *Acta Geologica Sinica* **78**, 358–65 (in Chinese with English abstract).

Zhang ZQ, Wang KX, Wang G, Liu XD, Liu WH and Wu B (2018) Petrogenesis and tectonic significances of the Paleozoic Jiling Syenite in the Mountain Longshou area, Gansu province. *Geological Review* **64**, 1017–29 (in Chinese with English abstract).

Zhao YY, Zhang SM, Tang L, Yao HF and Yang CS (2016) Sr-Nd-Pb isotopic characteristics and its geological significance of the Jiling Grantic Pluton in the Middle Longshou Mountains. *Earth Science* **41**, 1016–30 (in Chinese with English abstract).

Zheng YF, Chen YX, Dai LQ and Zhao ZF (2015) Developing plate tectonics theory from oceanic subduction zones to collisional orogens. *Science China Earth Sciences* **58**, 1045–69.

Zindler A and Hart S (1986) Chemical geodynamics. *Annual Review of Earth & Planetary Sciences* **14**, 493–571.

Zou HB, Zindler A, Xu XS and Qi Q (2000) Major, trace element, and Nd, Sr and Pb isotope studies of Cenozoic basalts in SE China: Mantle sources, regional variations, and tectonic significance. *Chemical Geology* **171**, 33–47.